FACULTY OF SCIENCE AND TECHNOLOGY

MASTER THESIS

Study program/specialization:
Mathematics and Physics/Physics

The spring semester, **2022**

Open

Author: **Mustansar Ali**

.....
(signature author)

Course coordinator: **Alex Bentley Nielsen**

Supervisor(s): **Olena Zavorotynska**

Thesis title:

Application of 2D correlation spectroscopy for in-situ Raman data analysis

Credits (ECTS): **60**

Keywords:

Pages: **65**

Raman spectroscopy
X-ray diffraction
Thermogravimetry
2D correlation

Stavanger, 15th June 2022

UNIVERSITY OF STAVANGER

DEPARTMENT OF MATHEMATICS AND PHYSICS

Application of 2D correlation Spectroscopy for in-situ Raman Data Analysis

Student:
Mustansar Ali

Supervisor:
Assoc. Prof. Olena Zavorotynska

June 15, 2022

Abstract

Two-dimensional correlation spectroscopy has become a valuable technique in the last decades. 2D spectroscopy is a tool to draw out the information from set of various data, which are acquired from the sample material under the influence of some external perturbation temperature, time, pressure and chemical excitation, etc. This chapter highlights the 2D correlation analysis of Ce-MOF-808 by applying temperature dependent perturbation. In addition to this, we applied the correlation technique on the preprocessed data of Mg(BH4)2 acquired by time-dependent perturbation at 140 ° C. The common way to obtain the information from Raman spectra to maps the synchronous and asynchronous spectra for deducing the molecular properties.

One of the main part of this work examine the crystal structure, site symmetry and vibrational analysis of $Mg(BH_4)_2$. Raman active species in isotopic exchange of $Mg(BH_4)_2$ and various methods are described here to find the selection rules for Raman active species. In addition to this Redlich-Teller product formula applied for calculating the vibrational frequency ratios in the isotopic shift of A_1 mode of BD_4 with repect to A_2 mode of BH_4. Raman spectra of Ce-MOF-808 and its precursors were obtained with green laser. Two sets of Raman spectra with temperature range 25 to 220° C and 200 to 450 ° C are acquired using red and green laser respectively to optimizing the measurement conditions for Raman spectroscopy.

Sample material analyzed by combined thermogravimetric analysis and differential scanning calorimetry, Raman spectroscopy and powdered X-ray diffraction. Decomposition of Ce-MOF-808 with temperature range 250-310 ° C was observed by thermogravometric analysis. Synchronous and asynchronous two-dimensional correlation maps of Raman dataset Ce-MOF-808 and Mg(BH4)2 were obtained using R language. For Ce-MOF-808 dataset acquired from Raman spectroscopy by employing temperature dependent perturbation, whereas in $Mg(BH_4)_2$ already acquired data utilize for correlation spectroscopic analysis.

Contents

Preface

The research presented in this thesis was conducted in the Department of Mathematics and Physics at the University of Stavanger Norway, under the supervision of Associate Professor Olena Zavorotynska. This research work completes the master's thesis go through 2021 autumn and 2022 spring semester. All measurements and data analysis of Ce-MOF-808 in the Master's thesis have been performed by me at UiS under the supervision Dr. Olena zavorotynska. However I did not perform the experiments on the isotopic exchange of magnesium borohydride. I have performed data analysis, including 2D correlation analysis, analysis of vibrational modes and Redlich-Teller spectroscopic rule. Thesis includes the Raman spectroscopy experiments, powder X-ray diffraction, thermogravimetry and 2D correlation analysis.

Mustansar Ali
15th July 2022
Stavanger, Norway

Acknowledgement

I would like to thank Tohoku University in Japan, group of prof. D.-I. Orimo, where the data on isotopic exchange in $Mg(BH_4)_2$ were collected. I would like to thank assoc. prof. S. Chavan from the UiS for providing the Ce-MOF sample analysis. I would like to express my thanks to my supervisor Dr. Olena zavorotynska, assoc. prof. in Mathematics and Physics department, UiS who supported me to complete this wonderful project "Application of 2D correlation spectroscopy for in-situ Raman data analysis" which helped me to do a lot of research to complete this project and learn new things. I consider myself as a lucky student to have such nice supervisor who continuously motivated me and guided with research articles, books and laboratory instruments during the whole thesis project and always welcomed me with smiling face. It would be unfeasible to complete my thesis project without assistance of my kind supervisor.

A heartful thank to my family especially for my elder brother, Mr. Masaud Ahmed Saqib who motivated and support me for the higher education to foreign country. Also appreciated my brother Mr. Mohsin Ali who inspired and create curiosity for physics since my graduation.

I would like to acknowledge the assistance that I received from post-doctoral colleague Sofiia Bercha for the support in collecting the Raman data. I would like to express my gratitude for all the professors at the department of Mathematics and Physics at UiS who teach me various courses of physics to improve my knowledge. Thanks goes on assoc. prof.essor Diana Lucia Quintero for enlightening the seminars and international conferences during my two years studies. Moreover, I'm also grateful to Ali Gohar for typesetting my thesis on Latex.

Mustansar Ali

Chapter 1

Introduction

1.1 Purpose

This thesis aimed at studying the application of 2D correlation analysis of complex in-situ Raman data. Furthermore, to understand the basic concept of correlation analysis. To analyse how similar or dissimilar spectral signals behave on applying perturbation (Temperature). Application of programming language to build the 2D correlation plots. Also try to learn about Ce-MOF-808 and its precursors using blue, green and red lasers with Raman spectroscopy. A significant portion of this work includes experimental analysis of Ce-MOF-808 using Raman microscope, X-ray diffraction (XRD), combined thermogravimetric analysis (TGA) and differential scanning calorimetry (DSC) to process and analyze the obtained data.

1.2 Objectives

In this work, two series of in-situ Raman data: i) decomposition of Ce-MOF at varying temperature and ii) isothermal isotopic exchange at varying time were analysed with 2D correlation approach. This thesis will also study synchronous and asynchronous spectra, auto and cross-correlation peaks and spectral signal changes after perturbation on Ce-MOF-808. Furthermore, H-D exchange in $Mg(BH_4)_2$ at 140 $^\circ$ with time was analysed with 2D correlation analysis. Here the analysis was compared/corroborated with analysis of H-B-D normal modes upon symmetry lowering and Redlich-Teller isotopic rule. Throughout the whole thesis, the main points are expected to be fulfilled:

- Implementation of 2D correlation method for the analysis of in-situ Raman data of Ce-MOF decomposition.
- Comparing the results with TGA-DSC analysis and assigning spectral features on the functional groups in MOFs.
- Theoretical and calculated approach to understanding the Mg(BH4)2 and its isotopes.
- To acuire practical experimental skills performing analysis with Raman, powder X-ray diffraction and DSC-TGA techniques.
- Analysis of XRD pattern of Ce-MOF and decomposed Ce-MOF.

1.3 Background

Spectroscopic techniques like infrared (IR), Raman or nuclear magnetic resonance are used to gain information about atoms and molecules. The standard way to take out information from Raman spectra is to assign the spectral signals to the molecular groups and determine the molecular properties such as chemical, physical and structural properties of molecules. However, sometimes it becomes hard to identify the spectral changes for the two overlapping signals in the series of spectra, making it impossible to assign these signals to a specific molecular group. To overcome this difficulty, thus 2D correlation analysis was invented. The fundamental objective of 2D correlation is to analyze how similar or dissimilar two spectral signals vary. A series of spectra collected under the external perturbation (temperature,T, pressure,p, pH level,time, t etc.) and a quantitative comparison of spectral intensities is observed [1]. 2-dimensional correlation analysis is derived from the 2D nuclear magnetic resonance spectroscopy and developed by Isao Noda in the 1980s for the application to various spectroscopic data. In 1993, 2D correlation extended its application because of its development based on Fourier transformation of data. Nowadays, 2D correlation analysis plays a significant role in interpreting different types of spectroscopic data (as such ultra Violet, fluorescence, infrared and Raman)[2].

Using 2D correlation analysis, someone can determine the specific positions in the measured signal where systematic changes occur, either continuously increasing or decreasing peak intensity [3]. The experiments built on physical correlation processes during the respective spectroscopic measurements are associated with 2D correlation spectroscopy. 2D correlation spectroscopy correlates spectroscopic data after the measurement. At the same time, 2D NMR and IR experiments generate the correlation during the info collection by unique experimental setups [1]. Two complementary outcomes of correlation analysis are synchronous and asynchronous spectra. These signals allow: us;[4]

1. To determine in-phase (events that co-occur) and out-phase (events that occur at different times) events.
2. To determine the inter and intra-molecular interaction in the sample material.
3. To find the sequence in the spectral variation.
4. To detect the correlations between the Raman spectroscopy.

2D correlation analysis was applied in this thesis to analyse in-situ Raman data collected on two examples, magnesium borohydride and cerium MOF. In the first case, the data were obtained at a constant temperature with time as an external perturbation. In the second case, the data were obtained as a function of temperature while heating and decomposing the sample. Magnesium borohydride is one of the most attractive hydrides for hydrogen storage and magnesium batteries. It has one of the highest hydrogen densities (14.8 wt % H), lower stability and releasing hydrogen. In order to determine which complex borohydride is most attractive as storage material, we must study the properties of borohydride that depends on the stability of (BH_4^{-1}) ion. The stability of (BH_4^{-1}) or B-H bond can be studied by vibrational spectroscopy. It can be investigate with isotopic exchange H $\rightarrow$ D, as such exchange would previsage breaking of the B-H and formation of thje B-D bonds. In fact, the temperature and rates of isotopic exchange was found to correlate with the decomposition temperature of borohydrides. Isotopically labelled borohydrides can be used to study hydrogen diffusion and thus it is important to assign peaks

in Raman spectra to various B-H or B-D containing molecular species. The (BH_4^{-1}) ion stability was investigated concerning H $\rightarrow$ D exchange. Ex-situ measurement of porous $(BH_4)_2$ indicates that the porosity of hydride is the focal reason behind the high isotropic exchange rates.

Free BH_4^- ions have T_d symmetry and four normal mode of vibrations: symmetric stretching and bending, v_1 (A1, Raman active) and v_2(E, R); asymmetric stretching and bending, v_3 (F_2, I.R ,R) and v_4 (F_2, R) . [5]. Whereas F is triply degenerate mode, so during H-D substitution and symmetry lowering, it is expected to split that will complicate the spectra and assignment.

The second system studied in this thesis is Ce-MOF. In-situ Raman data were obtained while decomposing Ce-808 MOF at RT to 450 $^\circ$ temperature range. The decomposition process was also followed by TGA-DSC in order to have a better understanding of various spectral events at different temperatures. The structure of MOF was analysed by powder XRD before and after TGA analysis. MOF are organic\inorganic hybrid crystalline porous materials that consist of a regular array of positively charged metal ions surrounded by organic 'linker' molecules. The metal ions tie up the arms of the linkers together to form a repeating, cage-like structure. Due to this hollow structure, MOFs have an extensive internal surface area. [6].

Depending on the application , MOFs should process one or several of the following properties:

- MOFs must have the proper surface area for host uptake and release the analytes.
- They need to exhibit reasonable stability upon exposure to oxygen, moisture or temperature.
- MOFs with a high surface area are desirable.
- They exhibit unique structural characteristics that will facilitate selective uptake and release of analytes.

In this thesis, we assessed the thermal stability of the Ce-808MOF. Ce-MOF-808 has space group $Fd-3m$. Before decomposition, it was revealed that decomposition, Ce-MOF-808, showed sizeable specific surface areas of 469.4 m^2/g, consisting of inorganic Ce-O clusters and organic linkers that contain phenyl rings. Ce-MOF-808 is made up of $[CeO_4(\mu - OH)4(OH)6(H2O)6(BTC)2]nH2O$, which contains the clusters and BTC3- linkers, in which each Cerium is connected to six BTC3- ligands and each BTC3-ligand further linked to three cerium clusters to give a 3D framework containing two groups of cages. One is a tetrahedral cage with a diameter of 4.8 A°, and the other is a diamond-shaped cage with a diameter of 18 A°. [7]. Thus the vibrational modes of the corresponding molecular group's clusters can be expected. Ce-MOF-808 is the stable MOF due to high intrinsic peroxidase-like catalytic activity under alkine, natural and neutral conditions. The catalytic activity of MOF-808 could be attributed to Ce-OH(OH2) groups. MOF-808 exhibit remarkably catalytic performance under the acidic and neutral reaction conditions, because of which it becomes favourable in biological systems.

Chapter 2

Mathematical basis of the 2D correlation method

2.1 2D correlation analysis

Two-dimensional correlation analysis is a mathematical technique where spectral intensity is plotted as a function of two independent variables. The independent variables are wavelength, wave number or frequency. In 2D spectroscopy, we put a sample in the system and then apply perturbation to stimulate the changes in the system. The system's response to perturbation manifests in its characteristic variation in the dynamic spectra. Dynamic spectra are the function of temperature, concentration, pressure, stress, electrical field, etc. Each perturbation effect uniquely and selectively depends upon the interaction with the matter and response of constituent particles [8]. A working principal of 2D correlation analysis is plotted on the figure 2.1.

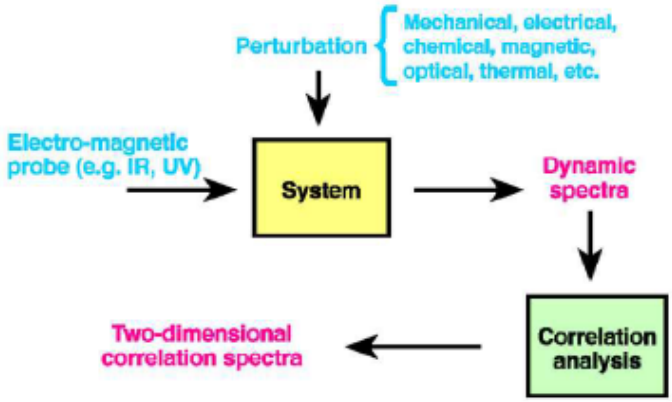

Figure 2.1: General scheme for 2D correlation spectrum [9]

2.1.1 Calculation of 2D spectra

Consider a perturbation applied on the spectra induced the variation in the spectral intensity $y(v,t)$ during the interval T_{max} and T_{min}. While t is an external variable measure the physical quantity, such as pressure, temperature and voltage etc. and 'v' is the spectral variable in spectroscopy e.g. Raman shift, wavenumber,

IR and UV wavelength etc. On applying perturbation, the dynamic spectrum $\tilde{y}$(v,t) of a system defined as [8]

$$\tilde{y}(v,t) = \begin{cases} y(v,t) - \tilde{y}(v) \\ T_{min} \leq t \leq T_{max} \\ 0, \qquad\qquad\qquad \text{otherwise} \end{cases}$$

Where $\tilde{y}$(v) is reference spectrum of the system. In practice 2D correlation spectroscopy is the quantitative comparison of spectral intensity variations observed at two different spectral variables between T_{max} and T_{min}. 2D correlation intensity X(v_1,v_2) can be treated as complex number that consist of two orthogonal components i.e real (synchronous) and imaginary (asynchronous) component [2].

$$X(v_1 v_2) = \phi(v_1, v_2) + \iota\, \psi(v_1, v_2) \tag{2.1}$$

2.1.2 Synchronous spectrum

Synchronous spectrum(map) is a symmetric spectrum with respect to the diagonal line. In synchronous 2D correlation, the intensity of spectrum ϕ (v_1, v_2) represents the coincidental change in intensity at v_1 and v_2. In case of synchronous spectra

$$\phi(v_1, v_2) = \frac{1}{n-1} y^T(v_1)(v_2) \tag{2.2}$$

Where:

- ϕ is the 2D synchronous spectrum
- y is a vector compose of signal intensity
- n is the number of signals in the dataset
- v_1 and v_2 are the two spectral channels
- y^T is the transpose of y.

Properties

The peaks located at diagonal positions correspond mathematically to the autocorrelated function; such diagonal peaks are referred to as auto peaks. For example, in the fig below, the peaks at spectral coordinates A, B, C and D are the autocorrelated peaks. The magnitude of autocorrelated peaks is always positive, showing the overall extent of spectral intensity at the spectral variable. Briefly, autocorrelated peaks exhibit the overall susceptibility of the spectral region to change in the intensity as an external perturbation is applied to the system [8].

The peaks which are located at the off-diagonal positions of a synchronous 2D map spectrum called cross-peaks. Cross-correlation peaks represent the coincidental changes seen at two different spectral variables, ν_1 and ν_2. Using cross-correlation peaks, we can construct the correlation square by joining the cross-peaks located at opposite sides of the diagonal as shown in the Figure 2.2 [8].

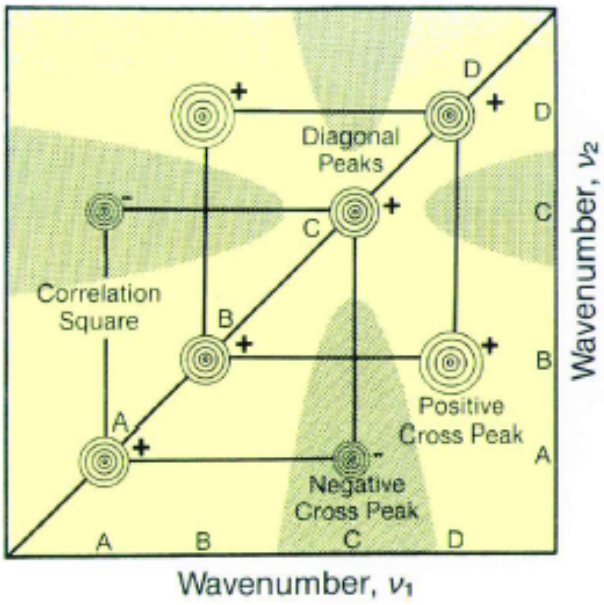

Figure 2.2: Synchronous 2D correlation spectrum[2]

2.1.3 Asynchronous spectrum

Asynchronous spectrum(map) is an anti-symmetric spectrum for the diagonal line. In asynchronous 2D correlation, the intensity of spectrum ϕ (v_1, v_2) represents the successive change in intensity at v_1 and v_2.

$$\psi(v_1, v_2) = \frac{1}{n-1}(v_1)N_i, jY(v_2) \tag{2.3}$$

$$N_{i,j} = \begin{cases} 0 & \text{if} j = k \\ \frac{1}{\pi(k-j)} & \text{otherwise} \end{cases} \tag{2.4}$$

Where:

- ψ is the 2D synchronous spectrum
- y is a vector compose of signal intensity
- n is the number of signals in dataset
- v_1 and v_2 are the two spectral channels
- $N_{i,j}$ Noda-Hilbert transform matrix

Properties

Unlike the synchronous spectrum, an asynchronous spectrum has no autocorrelated peaks. However, the asynchronous spectrum has cross-correlation peaks located at off-diagonal positions. Therefore, using cross-correlation peaks, we can construct the correlation square by joining the crosspeaks located at opposite diagonal sides. For example, in the below figure 2.3, there are four band pairs, A and B, C and D, B and C, and A and D can be observed. Thus using these cross-correlation peaks, it is possible to make four asynchronous correlation squares [8].

In the case of the asynchronous spectrum, crosspeaks evolve only if the intensities of the two spectra change out of phase. Such characteristics of asynchronous cross-peaks are fundamental in differentiating the overlapped bands developed from spectral signals of different origins [8].

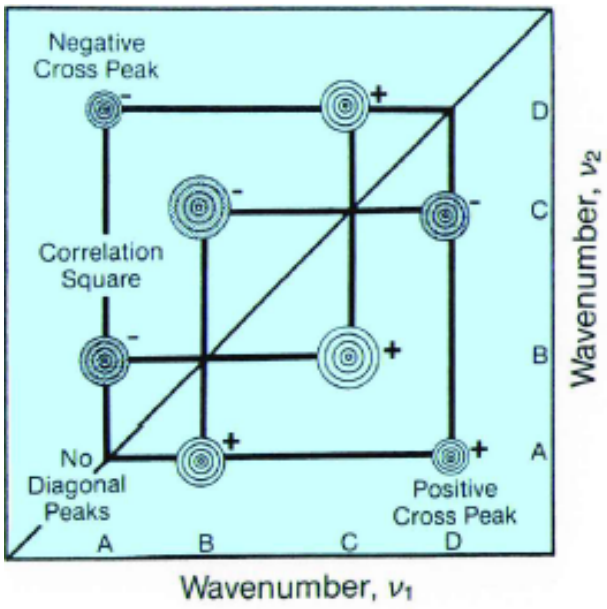

Figure 2.3: Asynchronous correlation spectra[2]

2.1.4 Interpretation of peaks

Following Noda rules are applicable for interpreting synchronous and asynchronous spectra [2][8].

- A sign of auto peaks is always positive. However, the sign of cross-peaks may be positive or negative.
- In a synchronous 2D correlation spectrum, if the intensity of the signals at v_1 and v_2 varies in the same direction, i.e. both intensities are increasing or decreasing simultaneously, there is a positive cross peak at $\phi(v_1,v_2)$.
- In a synchronous 2D correlation spectrum, if the intensity of the signals at v_1 and v_2 varies in the opposite direction, i.e. one is increasing, and the other is decreasing, there is a negative cross peak at $\phi(v_1,v_2)$.
- The intensity of the diagonal peaks is directly proportional to the intensity change in the original spectra.
- In the asynchronous spectrum, if the intensity of the signal change predominantly at v_1 before v_2, there is a positive cross peak at $\Psi(v_1,v_2)$.
- In the asynchronous spectrum, if the intensity of the signal change predominantly at v_2 before v_1, there is a negative cross peak at $\psi(v_1,v_2)$.

2.2 Raman Spectroscopy

Raman spectroscopy is typically used to determine vibrational modes, composition, materials and structure identification. Raman spectroscopy involves inelastic scattering of photons, known as Raman scattering. A source of monochromatic light, usually a laser light in visible, near Infrared, or UV region can be used The light interacts with the molecular vibrations or phonons in the system, resulting in the energy of the photons being shifted up or down depending upon the molecule's chemical structure. Most of the scattered light is at the same wavelength as the laser source and does not provide useful information – this is called Rayleigh Scattering. However, a small amount of light is scattered at different wavelengths, this is called Raman Scattering. The energy shift gives information about the vibrational modes and provides a structural fingerprint by which molecules can be identified. Sir Chandrasekhar Venkata Raman discovered this phenomenon in 1928, called the Raman effect. Sir C. V. Raman won the 1930 Nobel Prize in Physics for his discovery[10]. The figure 2.4 shows the Raman principle.

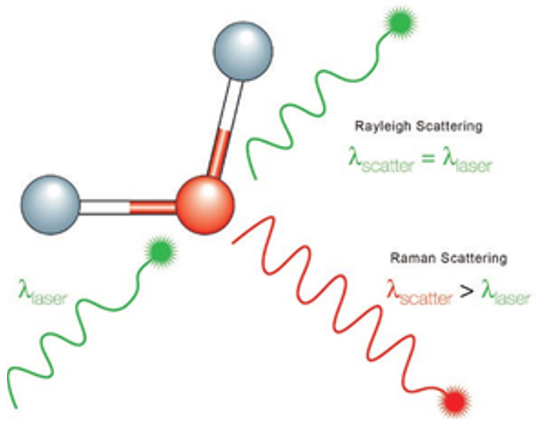

Figure 2.4: Raman Principle[10]

2.2.1 Origin of molecular spectra

In molecular spectra, the radiation spectrum is due to electrons' transition and quantum energy changes with molecules. Thus, the molecular spectrum consists of three components 1) Electronic motion in the molecule, 2) Vibration of constituent atoms, and 3) Molecular rotation. Thus, the total energy of the molecule will be

$$E_{tot} = E_{el} + E_{vib} + E_{rot} \tag{2.5}$$

Thus, if a molecule is placed in the electromagnetic field the energy changes according to Bohr's postulate will be $\Delta E = h\nu$, where ν is the frequency of electromagnetic radiation and h is Plank's constant. The physical origin of infrared and Raman spectra are markedly different. Infrared spectra originate because of the absorption of a photon in the IR region by transitions between two vibrational levels of the molecule in the electronic ground state. Suppose a molecule is irradiated by monochromatic light of frequency ν then because of induced electronic polarization in molecule cause scattered of this incident beam $\nu \pm \nu_i$. Thus the origin of Raman spectra is the shift of incident frequency in UV, IR and visible regions. In addition to what is above Raman spectra are generated because of the interaction between incident electromagnetic waves and vibrational energy levels of the molecule in the sample [11]. Different regions of spectrum are shown in the figure 2.5

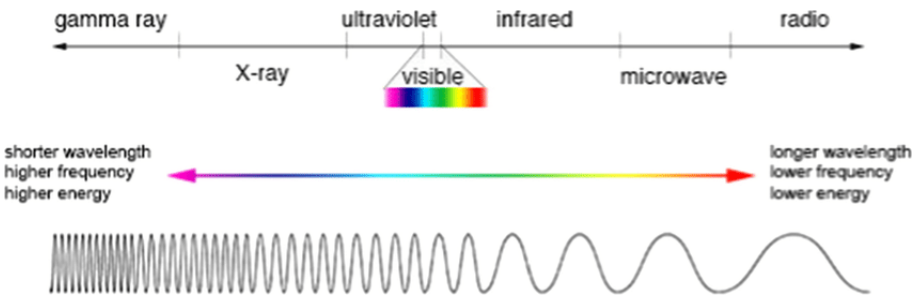

Figure 2.5: Electromagnetic spectrum[12]

In order to understand Raman spectroscopy we must understand some basic knowledge about light and properties.

2.2.2 Properties of light

Light is a form of electromagnetic radiation. According to Louis de Broglie, light behaves in particle (Photon) and wave nature properties. Mathematically can be described by the cosine function whose x parameter characterises the wavelength (distance between two consecutive wave crests or troughs), and the y parameter shows amplitude (height of the waves) [13].

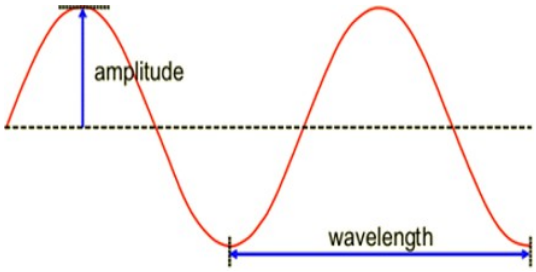

Figure 2.6: Light as a wave[14]

As light is the form of electromagnetic radiation, so it propagate like wave with certain amount of electromagnetic energy.If λ is wavelength and "c" speed of light then frequency ν is

$$\nu = \frac{c}{\lambda} \tag{2.6}$$

Similarly, this electromagnetic radiation contain energy E proportion to frequency ν and inverse with wavelength λ

$$E \propto \nu \propto \frac{1}{\lambda} \tag{2.7}$$

Equation 2.6 is valid only for a single light wave or photon. However, we know that light consists of many waves with different frequencies propagating in the same direction. Each frequency contributes to the beam with an intensity (i.e. a certain number of photons per time interval). The intensity of a light beam is the quantity that is ultimately measured with the detector of a spectrometer. The intensity distribution of all frequencies is called the spectrum of this light beam.

2.2.3 Light-matter interaction

When a light beam hits matter, it will interact with it specifically, dependent on the interplay between the light waves and the atoms and molecules that make up the matter. This interaction may leave the energy of matter and light unchanged or lead to energy exchange between both. However, there is an energy exchange between matter and light in spectroscopic analysis. The transfer of energy from light to matter leads to an excitation. In order to understand Raman spectroscopy, we prerequisite the knowledge of absorption, fluorescence, and scattering [15]. When light interacts with the matter, the sample absorbs some parts, and the remaining part is partially transmitted. In absorption, the frequency of an incoming light wave is at or near the energy level of electrons in the matter. The electrons will absorb light wave energy and change their energy state.

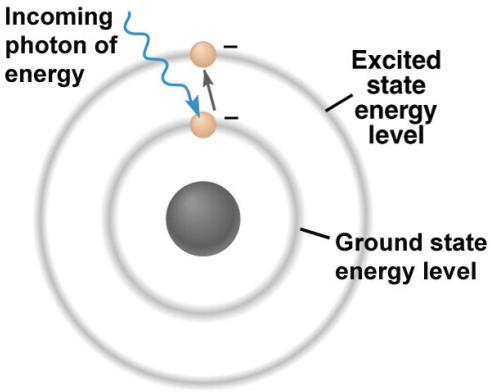

Figure 2.7: Excitation of e^- by photon(light)[16]

Matter can reemit absorbed light again by an independent process called fluorescence. In fluorescence, matter absorbs the light with shorter wavelength(high energy) and then reemits it with a longer wavelength(low energy) because some of its energy utilize in the excitation of an electron from the ground state to a higher state. There are certain materials which produce fluorescence by absorption of light [16].

Raman scattering

When an intense beam of light hits, the matter causes a change in the direction of incoming rays and the exchange of energy between the light and sample material called Raman scattering. Raman scattering is an inelastic scattering (the kinetic energy of an incident particle is not conserved). Thus change in the energy of scattered light results in changes in the frequency and wavelength. Inelastic scattering is the excitation and de-excitation of molecular vibration in the sample material. Thus, the scattered light spectrum gives information about the substance's vibrational structure. Thus, the above processes apply to extract information about the chemical and physical structure of the material. They can be used for vibrational spectroscopic analysis of the materials. Raman scattering is further subdivided into stokes Raman scattering and anti-stokes Raman scattering [17].

Stokes and Anti-stokes Scattering

Stokes Raman scattering is inelastic in which photons of light transfer their energy to the vibrating molecule. As a result, the scattered photon has less energy than the incident photon. Thus, the scattered

photon has lower energy and longer wavelength than the incident photon. The change in the energy of scattered light depends upon the material type and vibration of the molecule.

Anti-stokes Raman scattering is an inelastic Raman scattering in which vibrating molecules transfer their energy to the incoming photons. Thus, the scattered photon has more energy and less wavelength than the incident photon because there is an addition of energy from the vibrating molecule. Anti-stoke lines are weaker than stokes because there are many more molecules in the ground state than in an excited vibrational state. Furthermore, stokes Raman scattering is more intense than anti-stokes Raman scattering because the number of atoms in the ground state is more than the number in the excited states.

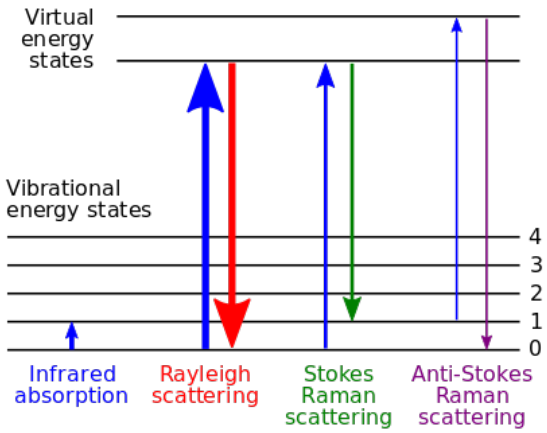

Figure 2.8: Energy diagram of Raleigh and Raman scattering [18]

Rayleigh Scattering

Rayleigh scattering is an elastic scattering of light by the molecule in which incident and scattered photon energy are conserved. In Rayleigh, scattering energy and wavelength of the incident and scattered photon does not change. In the Raman microscope, filters remove the rayleigh part from the signal to get the purify signal on the screen that provides more accurate information [19].

Table 2.1: Table 2.1: Shows the comparison of Rayleigh, stokes and anti-stokes Raman scattering

	Rayleigh	**Stokes**	**Anti-stokes**
Scattering is	elastic	inelastic	inelastic
Energy transfer	none	photon → molecule	molecule → photon
Effect on molecule	None	Excitation of vibration	De-excitation of pre-excitation vibrations
Effect on photon	change in direction same wavelength	change in direction higher wavelength	change in direction lower wavelength
Probability of occurance	common	very rare	extremely rare

Raman shift

The Raman shift is the energy difference between the incident (laser) and the scattered light. In Raman spectra, shifting of peaks towards lower or higher wave numbers depends on the molecule's chemical bond length. The longer bond length cause to shift the lower wavenumber. In comparison, shorter bond length

causes the shift in higher wavenumber. Raman shift is expressed in wave number whose unit is inverse of wavelength and is independent of laser wavelength. In order to convert between spectral wavelength and wavenumbers of the shift in the Raman spectrum, the following formula can be used

$$\Delta\tilde{\nu} = \left(\frac{1}{\lambda_0} - \frac{1}{\lambda_1}\right) \tag{2.8}$$

In above equation $\Delta\tilde{\nu}$ is Raman shift in wavenumber, λ_0 is an excitation wavelength and λ_1 raman spectrum wavelength. Generally we use the unit for raman shift is inverse of centimeter cm^{-1} whereas the wavelength of instrument is scaling in nanometer.Thus above equation can be modified

$$\Delta\tilde{\nu}(cm^{-1}) = \left(\frac{1}{\lambda_0(nm)} - \frac{1}{\lambda_1(nm)}\right) \times \frac{(10^7 nm)}{(cm)} \tag{2.9}$$

2.2.4 Sample analysis with Raman

In order to analyse the sample material, there is a particular time that needs the Raman to produce spectra called acquisition time. The acquisition time depends on the sample, instrument quality, and desired spectra. With the development in the instrument acquisition, time reduce. Acquisition time also depends on the number of data points. For the sample analysis, we focus on the laser spot whose size is defined by the laser wavelength and microscope objective. Using the Raleigh criterion, the microscope's resolution is defined as the minimum distance between two point sources such that their presence can be distinguished in the image.

$$\text{Laser spot diameter} = 1.22\frac{\lambda}{D} \tag{2.10}$$

where λ is the wavelength of the laser, and D is the numerical aperture of the microscope objective being used.From the above equation, it can be seen that lower wavelength lasers offer higher spatial resolution.Thus, blue laser with 488 nm will have a smaller spot size than red laser at 785 nm if we use the same objective.Standard Raman microscopes are limited to spot sizes in the order of 0.5-10 μm use.

2.2.5 Instrumentation

Because of a poor light source and weak detectors, acquiring the spectra took hours or days. Various colored filters and chemical solutions selected certain wavelength regions for excitation and detection. Raman and Krishnan used a mercury lamp and photographic plates to record spectra. However, modern Raman spectroscopy involves using lasers as excitation light sources. Advancements in science and technology have made our measurements more accurate and sensitive. Nowadays, charged couple devices are used as modern detectors in Raman microscope [20].

Laser

In modern Raman, spectrometer lasers are used as photon sources due to their high monochromatic nature and intense beam. In our experiment, we use three different lasers: blue, green, and red with 488 nm, 532 nm, and 633 nm, respectively. Generally, shorter wavelength lasers give stronger Raman scattering due to the increase in Raman scattering cross-sections. However, it may cause material damage or create fluorescence in our sample. So which laser we have to use in our experiment depends on the sample

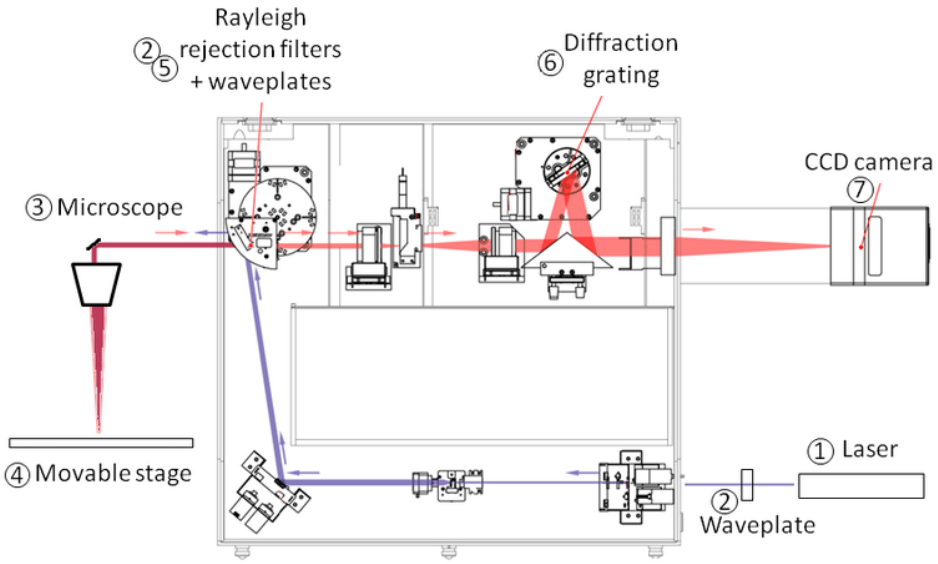

Figure 2.9: Internal Components of Raman spectroscopy [21]

material. Raman spectroscopy with longer wavelengths is preferred for samples suffering from high fluorescence backgrounds.

Detectors

In modern Raman spectrometers, CCDs (Charged-coupled devices) are used to detect the signals. A charged-coupled device is a silicon-based sensor comprising a silicon substrate and epitaxial layer. An integrated circuit is designed onto the silicon surface to make an array of pixels, which count the number of incoming photons and convert them to photoelectrons. CCDs can be used for weak signals or pulsed lasers.

Diffraction grating

The diffraction grating is used to separate the consistent wavelengths of the collected Raman scatter on different pixels of the CCD camera. Therefore, selecting the correct grating is essential in obtaining the best spectral results for the application.

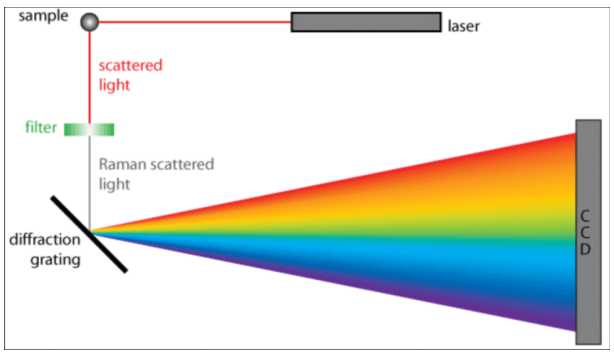

Figure 2.10: Diffraction grating[22]

Filters

It is usually necessary to separate the Raman scattered light from the Rayleigh and reflected laser signals to collect high-quality Raman spectra using a laser rejection filter. For this purpose, optical filters are placed in the Raman beam path and are used to block the laser line (Rayleigh scatter) selectively whilst allowing the Raman scattered light through to the spectrometer and detector. Each laser wavelength requires an individual filter.

2.2.6 Selection rule for Raman spectra

In Raman, there is a scattering of light by vibrating molecule, whereas in infrared, there is the absorption of light by vibrating molecule. In order to determine whether either vibration is Raman active or IR active selection rule should be applied.

Classical method

According to elementary classical theory the electric field strength 'E' of a light wave contain frequency 'ν' is given as $E = E_0 cos 2\pi vt$. Induced dipole moment of diatomic molecule placed in this field E is $P = \alpha E = \alpha E_0 cos 2\pi vt$ Now if molecule is vibrating with frequency v_i then displacement will be $q = q_0 cos 2\pi v_i t$. For small amplitude polarizability is linear function of displacement is $\alpha = \alpha_0 + \frac{\partial \alpha}{\partial q} q$ Now combining above two equations we get

$$P = \alpha E_0 cos 2\pi vt = \alpha_0 E_0 cos 2\pi vt + \frac{(\partial \alpha)_0}{\partial q} E_0 q_0 cos 2\pi v_i t cos 2\pi vt \tag{2.11}$$

$$P = \alpha E_0 cos 2\pi vt = \alpha_0 E_0 cos 2\pi vt + \frac{1}{2} \frac{(\partial \alpha)_0}{\partial q} E_0 q_0 \{cos[2\pi(v + v_i)t] + cos[2\pi(v - v_i)t] \tag{2.12}$$

In the above equation first term describes oscillating dipole that radiate light frequency. (Rayleigh scattering). Second term describe Raman scattering i.e. Stoke ($\nu + \nu_i$) and Anti-stoke ($\nu - \nu_i$)

- If $\frac{(\partial \alpha)_0}{\partial q}$ is not zero, it means there is change in polarizability, thus the vibration is Raman active.This is selection rule for Raman spectra.
- For a molecule to be IR active there must be a change in dipole moment. As the dipole moment is vector quantity depends upon magnitude and orientation. Thus, if any one of these (magnitude, orientation) is changing , molecule will be IR active.

Polarizability method

Polarizabily is the tendency of matter to gain the electric dipole moment when subjected to an electric field proportional to the applied field. We can find whether either vibration is Raman active or infrared active using the following rules [11].

1. Raman active: If any of the component of polarizability along the axis is changed during the vibration, in such vibrations there is Raman-active. Generally, the vibrations of homopolar diatomic molecule is Raman-active. For example O_2, N_2 and H_2. In water molecule v_1 ,v_2 vibration is Raman active because polarizability (size or shape of molecule) is change during vibration.

2. IR active: If there is a change in the dipole moment during the vibration, then there will be IR active. It is seen that generally, heteroatomic molecules are infrared active. water molecule, IR is active because

magnitude or direction is changed during vibration. If we write the dipole moment and their components in matrix form

$$\begin{bmatrix} P_x \\ P_y \\ P_x \end{bmatrix} = \begin{bmatrix} a_{xx} & a_{xy} & a_{xz} \\ a_{yx} & a_{yy} & a_{yz} \\ a_{zx} & a_{zy} & a_{zz} \end{bmatrix} \begin{bmatrix} E_x \\ E_y \\ E_z \end{bmatrix}$$

then component is the polarizability tensor $\begin{bmatrix} a_{xx} & a_{xy} & a_{xz} \\ a_{yx} & a_{yy} & a_{yz} \\ a_{zx} & a_{zy} & a_{zz} \end{bmatrix}$

Character table method

A character table is a 2-dimensional chart associated with a point group containing the irreducible representations of each point group and their corresponding matrix characters. In a character table, if representation cannot be simplified further called irreducible representation. Irreducible representations are obtained using the reduction formula. For example, we can find whether vibrational modes are IR active or Raman active using the character table [11].

- IR active: To be IR (allowed) active, vibration must change the dipole moment of the molecule. Only irreducible representations with x, y, z symmetry do this.
- Raman active: To be Raman active (allowed) vibration must change polarizability of molecule. Only irreducible representations that transform like binary products of (i.e.x^2,y^2, z^2) do this.

Quantum mechanics method

According to Quantum Mechanics selection rule for Raman spectrum is determined by the following integral

$$[\alpha]_{v\prime v\prime\prime} = \int \Psi_v^{*}\prime(Q_a)\alpha\psi_v^{"}(Q_a)dQ_a \tag{2.13}$$

Where α is dipole moment, ψ is wave function,Q_a is generalize coordinate of vibrational mode, $'$ is quantum number before transition,$'$, quantum number after quantum transition. Above equation can be resolve into six components α_{xx} , α_{yy} , α_{zz}, α_{xy} ,α_{yz},α_{zx} Thus, substituting the components of dipole moment in equation 2.13 we get six equations If all the integrals in component equations are zero the vibration is Raman active. However any one of the component equation is not zero then vibration is Raman in-active.

2.3 Symmetry analysis

Symmetry is the physical feather of the system in the atoms, molecules or compounds unchanged after various transformations. A point, line or plane about which symmetry operations are is performed called symmetry elements. There are five symmetry elements as described below.

1. Identity symmetry: This symmetry is found in all objects. It is corresponding to an operation doing nothing to an object. Every object has an identity. This is simplest symmetry element.

2. Plane of symmetry: Any imaginary plane about which if we reflect the molecule through this plane and we get the same molecule (Identity) called plane of symmetry. So, plane of symmetry is reflection through the plane. They are further three types. i) Horizontal symmetry ii) Vertical symmetry iii) Dihedral symmetry

3. Center of symmetry: A point at center of the molecule such that a straight line draw through the center links a point on one face to a similar point on an opposite face. In center of symmetry reflection of every atom of a molecule through inversion center leads to indistinguishable orientation.

4. Proper axis symmetry: In proper axis of rotation a molecule is rotated through an angle $\frac{360^0}{n}$ about an axis and produce configuration indistinguishable from original one. A molecule may have two, three, four or higher axis of symmetry.

5. Improper axis symmetry: In improper axis of symmetry a molecule is rotated about an angle $\frac{360^0}{n}$ followed by reflection at plane perpendicular to the axis and produce configuration indistinguishable from original one. A molecule may have two, three, four or n-fold of symmetry.

2.3.1 Crystal structure and symmetry in $Mg(BH_4)_2$

$Mg(BH_4)_2$ has a number of polymorphs forms, which include α, β,β^- γ,ϵ,δ, and ζ $Mg(BH_4)_2$. However gamma phase $\gamma - Mg(BH_4)_2$ is a nanoporous hydride with high specific surface area i.e SSA > 1000 m^2g^{-1} and the pores have a diameter about 7Å. Other polymorphism and amorphous form of $Mg(BH_4)_2$ do not posses this unique high specific surface area. As $\gamma Mg(BH_4)_2$ contain space group Ia3d which is cubic structure [23]. And the cubic unit cell containing 24 units of $Mg(BH_4)_2$ structure of magnesium borohydride contain total number of molecules $Z = 24$ One molecule of $\gamma Mg(BH_4)_2$ contain atoms= $1+2+8$. Thus total number of atoms= $11*24 = 264$ Lattice parameters a=15.8234Å $\alpha = 90^\circ$ degree [24]

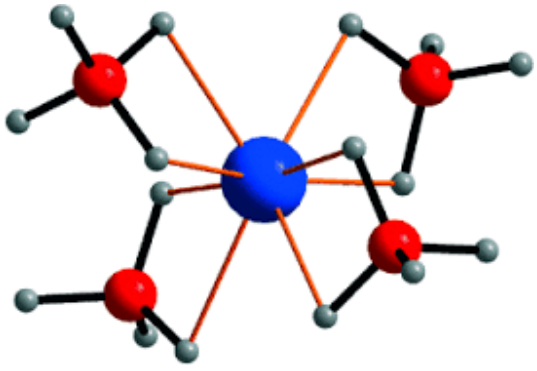

Figure 2.11: $Mg(BH_4)_2$ is complex 2D dimensional structure in which eachMg^{+2} ion (blue) is tetrahedrally coordinated by four BH_4 ions (Boron red, Hydrogen grey)[23].

Space group of $\gamma - Mg(BH_4)_2$

Group of all symmetry elements of crystal structure called space group. In 2D, there are 17 distinct groups, whereas, in 3D, there are 230 distinct groups. The symmetry of crystal structure is specified completely when the space group is known. There are six glide planes in the space group, i.e. a, b, c, d, e

and n. From the space group, we can determine bravais lattice, symmetry, point group, symmetry element, etc. Symmetry operations in the space group are a) Translation b) Reflection c) Rotation d) Inversion

The space group of $\gamma - Mg(BH_4)_2$ is $Ia3d$ which is cubic structure.The first term 'I' represent lattice type I =body centred , second term glide plane 'a' which is perpendicular to n. .Third one is mirror plane '3' means 3-fold rotation. The last one 'd' is glide plane which is perpendicular to c-axis.

Site symmmetry in $\gamma - Mg(BH_4)_2$

Site symmetry of molecular ion in the unit cell can be lowered with respect to the point group symmetry of the free molecule. This explains possible splitting of the degenerate mode and as a consequence, appearance of the additional modes in the spectra. The site symmetry should be a subgroup of the molecular symmetry. For example, the site symmetry of BH_4^{-1} ions in the $Mg(BH_4)_2$ should be the subgroup of the tetrahedral of free BH_4^{-1} ion, T_d. Tetrahedral borohydride ion shown in the figure 2.12. The site group symmetry of a point is the finite group formed by the set of all symmetry operations of a space group that leaves the point invariant. It is the subgroup of point group to which space group under consideration belongs. As $\gamma - Mg(BH_4)_2$ belongs to space group whose point symmetry is O_h^1. Thus possible site symmetry of $\gamma Mg(BH_4)_2$ are C_3i(8), D_3(8), D_2 (12), S_4 (12), C_3 (16) , $2C_2$ (24) and C_1 (48). Number in parenthesis denote number of distinct set of sites for each distinct (Z).

- There is one Magnesium atom in $\gamma - Mg(BH_4)_2$.
- There are two Boron atoms in $\gamma - Mg(BH_4)_2$.Thus site symmetry for boron is C_1 (48).

Point group of Borohydride

Various types of point groups are i) Low symmetry point group ii) Linear point group iii) Cyclic point group iv) Tetrahedral T_d v) Octahedral O_h
Borohydride belongs to tetrahedral T_d point group. Some symmetry elements in borohydrides are E, $3S_4$, $3C_2$, $4C_3$, and $6\sigma_d$.Point group of isotopically substituted borohydride ions.
BH_3D : C_{3v}
BH_2D_2: C_{2v}
BHD_3 : C_{3v}
BD_4 : T_d

2.3.2 Vibrational analysis

The vibrations of the molecule are said to be symmetric if all the atoms attach to molecule move/vibrate in the same direction. e.g. $v_1(A_1)$, v_2 (E) vibrations in the BH_4^{-1} are symmetric.Whereas an asymmetric stretch/bending occurs when some atoms move in the same direction while others move in the opposite direction. e.g. $v_3(F_2)$, $v_4(F_2)$ vibrations in the BH4 molecules are anti-symmetric. Consider a molecule having only one mode of vibration with kinetic as well as potential energy is

$$T = \frac{1}{2}\Sigma_i Q_i^2 \tag{2.14}$$

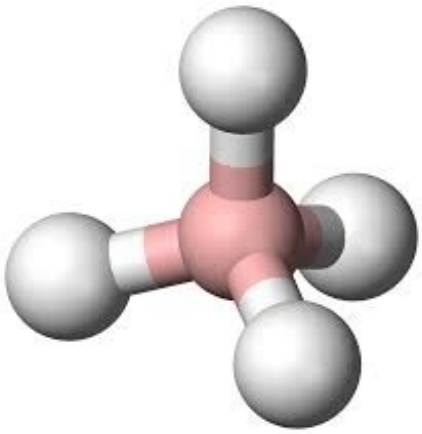

Figure 2.12: Tetrahedral borohydride ion [18]

$$V = \frac{1}{2}\lambda_i \Sigma_i \dot{Q_i}^2 \tag{2.15}$$

Where Q is Lagrange coordinate, λ is Lgrange multiplier. Energy of molecule must be invariant under the symmetry operation R , and coordinates changes from Q_i to RQ_i. Thus kinetic as well as potential energy will be

$$T = \frac{2}{2}\dot{Q_i}^2 = \frac{1}{2}(R\dot{Q_i})^2 \tag{2.16}$$

$$V = \frac{1}{2}\lambda_i Q_i^2 = \frac{1}{2}\lambda_i (RQ_i)^2 \tag{2.17}$$

Equation 2.16 and 2.17 holds only if $(R\dot{Q_i})^2 = Q_i^2$ or $RQ_i = \pm Q_i$.Now if $Q_i = RQ_i$ the vibration is said to be symmetric and $Q_i = -RQ_i$ non symmetric.

Totally and non-symmetry vibration

If a molecule preserves all symmetry properties during its vibration, it is said to be a total symmetry vibration. (This means the molecule does not lose its symmetry properties during its vibration). e.g. during $v_1(A_1)$ and $v_2(E)$, vibration BH_4^{-1} preserve all symmetric properties. However, the asymmetric vibration molecule loses its symmetry properties during its vibration. e.g. $v_3(F_2)$ and $v_4(F_2)$ vibrations in the BH_4^{-1} molecules lose some of their properties.

A typical mode of an oscillating system is a pattern of motion in which all parts of the system move sinusoidally with the same frequency and with a fixed phase relation. In a diatomic molecule, nuclei vibration occurs along the two nuclei line. However, the system's vibration becomes complex in the polyatomic molecule because each nucleus has individual oscillations. These complicated vibrations may be represented as the superposition of several normal vibrations. Thus kinetic energy for the N-atom molecule would be expressed as [11]

$$T = \frac{1}{2}\sum_N m_n \left[\left(\frac{d \triangle x_n}{dt} \right)^2 + \left(\frac{d \triangle y_n}{dt} \right)^2 + \left(\frac{d \triangle z_n}{dt} \right)^2 \right] \tag{2.18}$$

In generalize coordinates

$$q_1 = \sqrt{m_1 \triangle x_1},\ q_2 = \sqrt{m_2 \triangle y_1} \text{ and } q_3 = \sqrt{m_3 \triangle z_1}$$

Vibrations in BH_4 and $Mg(BH_4)_2$

A polyatomic molecule has following modes of vibration. For linear 3N-5 and non-linear 3N-6 where N is number of atoms in molecule. $(BH)_4$ is non-linear, thus number of vibrations in Borohydride are $3N - 6 = 3(5) - 6 = 9$. In case of $Mg(BH_4)_2$ the number of molecules in a unit cell $Z = 24$
Number of atoms in $Mg(BH_4)_2 = 1 + 8 + 2 = 11$
Thus, total number of atoms in motif $= 11 * 24 = 264$
Total number of vibrations $= 3N = 3(264) = 792$

2.3.3 Raman-active species in isotopically substituted of Borohydride ions

These space group can be represented by Hermann-Maugin and Schonflies notation.Meaning of Mulliken symbols that we use in our charter table is given below.

Table 2.2: Meaning of Mulliken symbols

Symbols	Description
A	Singly degenerate, symmetry with respect to principal axis
B	Singly degenerate, anti-symmetry with respect to principal axis
E	Doubly degenerate
F	Triply degenerate
g	Symmetric with respect to inversion through center
u	Anti-symmetric with respect to inversion through center
1	Symmetric with respect to additional rotation
2	Anti-symmetric with respect to additional rotation
'	Symmetric with respect to horizontal plane
"	Anti-symmetric with respect to horizontal plane

1. For BH_4

As BH_4 belongs to T_d point group, thus we use T_d charter table.A_1 , A_2, T_1, T_2 and E are the vibrational species of BH_4.As E, A_1 and T_2 are the quadratic coupling (binary product of x,y and z).Thus Raman Active species: A_1 , E and T_2

Table 2.3: Character table for T_d point group

T_d	**E**	**8**C_3	**3**C_2	**6**$6S_4$	**6**σ_d	Linear rotations	Quadratic
A_1	1	1	1	1	1		$x^2 + y^2 + z^2$
A_2	1	1	1	-1	-1		
E	2	-1	2	0	0		$(2z^2 - x^2 - y^2, x^2 - y^2)$
T_1	3	0	-1	1	-1	(R_x, R_y, R_z)	
T_2	3	0	-1	-1	1	(x, y, z)	(xz, yz, xy)

2. For BH_3D

As $(BH)_3D$ belongs to C_3v point group, thus we use C_3v charter table. A_1, A_2 and E are the vibrational species of $(BH)_3D$. As A_1 and E are the quadratic coupling (binary product of x,y and z).Thus Raman Active species: A_1 and E

Table 2.4: Character table for C_3v point group

C_3v	**E**	**2**C_3	**3**σ	Linear rotations	Quadratic
A_1	1	1	1	z	$x^2+y^2+z^2$
A_2	1	1	-1	R_z	
E	2	-1	0	(x,y)(R_x,R_y)	(x^2-y^2, xy)(xz,yz)

3. For BH_2D_2

As $(BH)_2D_2$ belongs to C_2v point group, thus we use C_2v charter table.A_1 , A_2 , B_1 and B_2 are the vibrational species of $(BH)_2D_2$. As A_1, A_2, B_1 and B_2 are quadratic comparing to charter table C_2v. Hence $(BH)_2D_2$ has Raman Active: A_1, A_2, B_1 and B_2

Table 2.5: Character table for C_2v point group

C_2v	**E**	$C_2(z)$	**3**$\sigma_v(xy)$	$\sigma_v(yz)$	Linear rotations	Quadratic
A_1	1	1	1	1	z	x^2, y^2, z^2
A_2	1	1	-1	-1	R_z	xy
B_1	1	-1	1	-1	xR_y	xz
B_2	1	-1	-1	1	y, R_x	yz

2.3.4 Vibrational modes

In order to calculate the total number of atoms and number of normal vibrational modes of each symmetry species we use the appendix III from Nakamoto [11]

Table 2.6: Molecular symmetry and number of vibrational modes of each symmetry

ion	point group	Total number of atoms	species	Number of vibrations	calculation
BH_4	T_d	24m+12m_d+6m_2 +4m_3+m_0	A_1	3m + 2 $m_d + m_2 + m_3$	A_1=0+0+0+1=1
			A_2	3m+m_d	A_2=0+0
			E	6m+3m_d+m_2+m_3	E=0+0+0+1=1
			F_1	9m+4m_d+2m_2+$m_3 - 1$	F_1=0+0+0+1-1=0
			F_2	9m+5m_d+3m_2+2m_3 +m_0-1	F_2=0+0+0 +2×1+1-1=2
BH_3D	C_{3v}	6m+ 3m_v + m_0	A_1	3m+2m_v +m_0-1	A_1=0+2+2-1=3
			A_2	3m+$m_v - 1$	A_2= 0+1-1=0
			E	6m+3m_v+m_0-2	E= 0+3+2-2=3
BH_2D_2	C_{2v}	4m+2m_{xz}+2m_{yz}+m_0	A_1	3m+2m_{xz}+2m_{yz} +m_0-1	A_1= 0+2+2 +1-1=4
			A_2	3m+m_{xz}+m_{yz}-1	A_2=0+1+1-1=1
			B_1	3m+2m_{xz}+m_{yz}+m_0-2	B_1=0+2+1+1-2=2
			B_2	3m+m_{xz}+2m_{yz}+m_0-2	B_2=0+1+2+1-2=2
BHD_3	C_{3v}	6m+3m_v+m_0	A_1	3m+2m_v+m_0-2	A_1=0+2+2-1=3
			A_2	3m+m_v-1	A_2=0+1-1=0
			E	6m+3m_v+m_0-2	E=0+3+2-2=3
BD_4	T_d	24m+12m_d+6m_2 +4m_3+m_0	A_1	3m+2m_d+m_2+m_3	A_1=0+0+0+0+1=1
			A_2	3m+m_d	A_2=0+0=0
			E	6m+3m_d+m_2+m_3	E=0+0+0+1=1
			F_1	9m+5m_d+m_2 +m_3-1	F_1=0+0+0 +1-1=0
			F_2	9m+5m_d+3m_2+2m_3 +m_0-1	F_2=0+0+0 +2+1-1=2

In the above table

A_1 , A_2 ,B_1 ,B_2: are non-degenerate species.

E_1 , E_2 are double degenerate species.

F_1 , F_2 are triply degenerate species

$m =$ Number of sets of nuclei not any element of symmetry

$m_d =$ Number of nuclei on σ_d plane but not on any other element of symmetry

$m_0 =$ Number of sets of nuclei on all elements of symmetry

$m_2 =$ Number of sets of nuclei on two-fold axis but not on any other element of symmetry

$m_3 =$ Number of sets of nuclei on 4-fold axis but not on any other element of symmetry

m_{xz}=numbers of sets of nuclei lying on the xz plane but not on any axes going through these planes

m_{yz}=numbers of sets of nuclei lying on the yz plane but not on any axes going through these planes

$m = 0 \qquad m_d = 0 \qquad m_0 = 1 \qquad m_2 = 0 \qquad m_3 = 1$

As BH_4^{-1} belongs to T_d symmetry, thus the normal modes of the substituted anions will be related to the vibrations of BH_4 as shown in the correlation table 2.6.

Table 2.7: Correlation table for BH_4^{-1} substituted anions

T_d	C_{3v}	C_{2v}
A_1	A_1	A_1
A_2	A_2	A_2
E	E	$A_1 + A_2$
F_1	$A_2 + E$	A_2+B_1+B_2
F_2	$A_1 + E$	A_1+B_1+B_2

Isotopic exchange in BH_4

In the first equation BH_4^- ion is most stable with highest T_d symmetry. However, during isotopic exchange hydronium atom is replaced with deuterium atom cause decrease its c_3v symmetry. As further isotopic exchange in $BH_3D^-_{(c_3v)}$ cause to reduce more symmetry. i.e $C_{3v} \rightarrow C_{2v}$. Thus, following exchange reaction takes place.

$$BH_4(T_d)^- + D_2 \rightarrow BH_3D^-_{(c_3v)} + HD \tag{2.19}$$

$$BH_3D^-_{(c_3v)} + D_2 \rightarrow BH_2D_2(c_2v) + HD \tag{2.20}$$

$$BH_2D_2(c_2v) + D_2 \rightarrow BHD_3(c_3v) + HD \tag{2.21}$$

$$BHD_3(c_3v) + D_2 \rightarrow BD_4(T_d) + HD \tag{2.22}$$

2.3.5 Redlich-Teller product formula

As we have shown above that the spectra of $Mg(BH_4)_2$ can become very complicated: with all the 700 vibrations in yhr unit cell plus, symmetry lowering and overtones upon H-D substitution. Plus new peaks are expected to emerge in the B-D regions. Redlich Teller rule can help in identifying and assigning these peaks. RT product formula is an important formula that we use to find the vibrational frequency ratios of an isotopes.We can also use this formula for calculating the shift in one molecule with respect to its isotope.

$$\frac{\tilde{v_1}.\tilde{v_2}....\tilde{v_n}}{\tilde{v_1'}\tilde{v_2'}....\tilde{v_n'}} = \sqrt{\left(\frac{m_1'}{m_1}\right)^{\alpha}\left(\frac{m_2'}{m_2}\right)^{\beta}.....\left(\frac{M_1}{M_1'}\right)^{t}\left(\frac{I_x}{I_x'}\right)^{\delta x}\left(\frac{I_y}{I_y'}\right)^{\delta y}\left(\frac{I_z}{I_z'}\right)^{\delta z}} \tag{2.23}$$

Here($'$) symbol mean same atom with isotope,$\tilde{v_1}$,$\tilde{v_2}$ vibrational frequency of atom, m_1, m_2.... are the masses of representative atoms of various set of equivalent nuclie ;α,β are the coefficients of m, m_0,m_{xy}...;M is total mass of molecule; t is the number of T_x, T_y and T_z in the symmetry type considered;I_x,I_y, I_z are the moment of inertia about x, y, z axes respectively, which go through the center of mass; and ∂_x, ∂_y, ∂_z are 1 to 0, depending on whether R_x, R_y, R_z belong to symmetry type considered.A degenerate vibration is counted only once on both sides of the equation.

Isotopic shift for H-H stretching bond

Here we use H2 and D2 molecule. In order to find isotopic shift for H-H stretching bond we have to find their vibrational frequencies ratio. Vibrational frequency for H_2 and D_2 is

$$V_{H_2} = \frac{1}{2\pi}\left(\frac{k}{\mu_{H_2}}\right)^{\frac{1}{2}} \tag{2.24}$$

$$V_{H_2} = \frac{1}{2\pi}\left(\frac{k}{\mu_{D_2}}\right)^{\frac{1}{2}} \tag{2.25}$$

$$\mu = \frac{m_1.m_2}{m_1 + m_2} \tag{2.26}$$

For deuterium atom

$$\mu_{D_1} = \frac{2.2}{2+2} = \frac{4}{4} = 1 \tag{2.27}$$

For hydrogen atom

$$\mu_{H_1} = \frac{1.1}{1+1} = \frac{1}{2} \tag{2.28}$$

$$\frac{v_{D_2}}{v_{H_2}} = \frac{\frac{1}{2\pi}\left(\frac{k}{\mu_{D_2}}\right)^{\frac{1}{2}}}{\frac{1}{2\pi}\left(\frac{k}{\mu_{H_2}}\right)^{\frac{1}{2}}} \tag{2.29}$$

In equation 2.29 $K =$ Bond force constant $\mu =$ Reduced mass K is same because of H_2 and D_2 have the same number of electrons.Substituting the values in above equation, we get

$$\frac{V_{D_2}}{V_{H_2}} = \left(\frac{1}{2}\right)^{\frac{1}{2}} = 0.707 \tag{2.30}$$

A1 mode of BD4 with respect to BH4

We will use Redlich-Teller product formula for calculating shift for A1 mode of BD4 with respect to BH4

$$\frac{A_1(BH_2)}{A_1(BD_4)} = \sqrt{\left(\frac{m_1'}{m_1}\right)^{\alpha}\left(\frac{m_2'}{m_2}\right)^{\beta}\left(\frac{M_1}{M_1'}\right)^{t}\left(\frac{I_x}{I_x'}\right)^{\delta x}\left(\frac{I_y}{I_y'}\right)^{\delta y}\left(\frac{I_z}{I_z'}\right)^{\delta z}} \tag{2.31}$$

$m_1' = m_1 = m(B) =$mass of boron because we use the same isotope of boron, $m_2' = m(D) = 2$, $m_2 = m(H) = 1$ $M =$ mass of BH4=10.8+4 =14.8 , $M' =$mass of BD4=10.8+8=18.8, $\alpha = \beta = 1$, $t = 0$ as from character table of T_d symmetry translations along x, y and z axis are zero. As R_x , R_y and R_z are zero from character table of T_d thus, δ_x, δ_y,$\delta_z = 0$ substituting values in above equation we get

$$\frac{A_1(BH_2)}{A_1(BD_4)} = \sqrt{\left(\frac{1}{1}\right)^{1}\left(\frac{2}{1}\right)^{1}\left(\frac{14.8}{18.8}\right)^{0}\left(\frac{I_x}{I_x'}\right)^{0}\left(\frac{I_y}{I_y'}\right)^{0}\left(\frac{I_z}{I_z'}\right)^{0}} = 1.4142 \tag{2.32}$$

Intensity ratio for A1 mode of BH_4 and BD_4

As BH_4 and BD_4 are tetrahedral molecule thus in order to find intensity ratio for A1 mode of BH_4 and BD_4 molecule, we use the following formula

$$\frac{I_1}{I_2} = \frac{C_1}{C_2}\left(\frac{V_0 - V_1}{V_0 - V_2}\right)^4 \frac{\mu_2 V_2}{\mu_1 V_1}\frac{\left(1 - e^{\frac{-hcv_2}{kT}}\right)}{\left(1 - e^{\frac{-hcv_2}{kT}}\right)}\left(\frac{\alpha_1}{\alpha_2}\right)^2 \tag{2.33}$$

For our convenient and to make the equation more generalize, we use the substitution 1: subscript for BH_4, 2: subscript for BD_4, α_1 Polarizability of BH_4, C_1 molar concentration in BH_4, v_1 vibrational quantum number and $\alpha_1 = \alpha_2 = \alpha$ polarizability is same because of same structure. $C_1 = C_2 = C$ Molar concentration is same as we are trying to find the intensity ratio for the same concentration of the BH4 and BD4 species, v_0 Excitation of laser wave length =532nm,$v_0 - v_1 =$ Raman shift

$= 2320cm^{-}1 = 4310.34nm$, $v_1 = -3778.34nm$,$v_0 - v_2 =$ Raman shift$= 1606cm^{-}1 = 6226.65.nm$, $v_2 = -5694.65nm$.And mass of Boron$= 1.00784\ a.m.u$, mass of Hydrogen$= 2.014\ a.m.u$,mass of Deuterium$= 10.811\ a.m.u\ K = 1.38 \times 10^{-23}m^2Kgs^{-2}K^{-1}$, $c = 3 \times 10^8ms^1, h = 6.62 \times 10^{-34}Kgm^2s^1$ and $T = 300K$.

$$\mu = \frac{m_1.m_2}{m_1 + m_2} \tag{2.34}$$

For BH_4 atom

$$\mu_1 = \frac{10.8 * 4}{10.8 + 4} = \frac{43.2}{14.8} = 2.918 \tag{2.35}$$

For BD_4 atom

$$\mu_2 = \frac{10.8 * 8}{10.8 + 8} = \frac{86.4}{18.8} = 4.59 \tag{2.36}$$

$$\frac{hcv_2}{KT} = -2.73 \times 10^{-10} \qquad \frac{hcv_1}{KT} = -1.81 \times 10^{-10} \tag{2.37}$$

$$e^{\frac{-hcv_2}{KT}} = 15.333A^o \qquad e^{\frac{-hcv_1}{KT}} = 6.1104A^o \tag{2.38}$$

$$\frac{I_1}{I_2} = \left(\frac{4310.34}{6226.6}\right) \frac{5694 \times 4.6}{3778 \times 2.9} \frac{(-14.333)}{(-5.1104)} = 1.5 \tag{2.39}$$

Group frequency and Raman Intensity

From the vibrational spectra(including infrared and Raman), it has been found that in many of the compounds, there is a collaborative group of atoms that absorb (in the case of infrared absorption) over a narrow range of energy. This energy range is called group frequency. For Example, the Methyl group exhibits symmetric and anti-symmetric stretching vibrations in 3050 -2950cm-1 and 2970-2860cm-1, respectively. So this is group velocity for symmetric and anti-symmetric stretching. Group frequency uses to identify the atomic group from observed spectra. The classical equation for Raman intensity is given as

$$I_n = const \left(\frac{\partial \alpha}{\partial Q}\right)^2 E^2 \tag{2.40}$$

Q : General coordinates, α Polarizability.Thus, the intensity of a Raman vibration depends on the change in the polarizability with respect to the change in the coordinates and the magnitude of the electromagnetic field. Using substitution modified form of Raman Intensity is given as

$$I_n = KI_0 \frac{(v_0 - v)^4}{\mu\nu(1 - e^{\frac{-h\nu}{KT}})}[45(\alpha)^2 + 13\gamma^2] \tag{2.41}$$

I_0 Incident light intensity, v_0 ground state, V= stoke transition (higher energy state), v stokes frequency,μ reduced mass, α Mean value of Polarizability, γ anisotropy (Properties of material depends upon direction) and K summarize all constants.

2.4 Powder X-ray diffraction

X-rays are the high energetic electromagnetic radiations with energy ranging from 100eV to 10MeV. Wavelengths of X-rays are shorter than Ultra-Violet and larger than gamma rays. Because of high energetic particles, they can pass through most the objects. The wavelength of X-rays is comparable to the size of atoms, so they can be used in crystallography in material science to explore the inner structure of materials.

X-rays can penetrate through the matter easily because of their high energy. As X-rays are electromagnetic waves, they can be explained by the electromagnetic theory of radiations(Maxwell equations). They show the properties of wave-like reflection, refraction and diffraction etc. Similarly, the particle nature of X-rays can be explained by quantum mechanics. As a particle nature, X-rays show photoelectric effect and absorption phenomena. Particle nature is proven by the Compton effect (Increase in the wavelength after scattering). Generally, low energetic photons behave like waves while high energetic photons behave like particles [25].

Crystals are the solid materials whose atoms are in the regular array(definite pattern) forming crystal lattice and extended in all direction. X-rays are energetic particles and atoms scattered with x-rays produce a definite pattern depends on the crystal structure. According to energy ranges, x-rays are classified as hard and soft x-rays. X-rays with high energy photons with a wavelength of more than 5-10KeV are called hard x-rays, while x-rays with lower energy wavelengths are usually known as soft x-rays. Because of their high energy and penetrating power, hard X-rays are widely used to visualise the inside objects. Furthermore, since the wavelength of hard x-rays is comparable to the size of atoms, thus they help determine the crystal structure. At the same time, soft x-rays are used to study the biological samples.

2.4.1 Bragg's Law

When the radiations have the wavelength λ comparable to the size of atomic spacing, such radiations scattered by the crystal lattice undergo the interference may be constructive or destructive depending upon the phase difference. If the scattered waves are out-of-phase, they interface destructively. However, if they are in phase, they interface constructively, and the diffracted pattern will be obtained on the screen [26] . Consider a crystalline solid, radiation with wavelength λ incident on the crystal whose atomic spacing between the atomic layers is d and glancing angle is θ, then

$$n\lambda = 2dsin\theta \tag{2.42}$$

In the above equation 'n' is the diffraction order $n = 1, 2, 3, 4...$ 'd' is inter-planning space i.e diffraction grating, λ is the wavelength of incident radiation and θ is the angle between incident wave and plane of the crystal. There is a path difference between upper and lower beam. Lower beam cover the extra path $2dsin\theta$. Above equation holds only if the path difference is the integral multiple of the wavelength, then there will be constructive interference and spot will be observed, however in case of destructive interference no spot can be seen on the screen[27]. Bragg's law describes the diffraction in scalar form while crystals are generally, three dimensional that needs to be express in vactor form. Consider one-dimensional array of atoms with inter-planning space 'a' between them. A beam $s - o$ is incident on the atom making an angle α_0 with atomic plane, and after diffracted it scattered with angle α. Thus according to Bragg's law path difference between the incident and reflected beam must be integral multiple of the wavelength.

$$a(cos\alpha - cos\alpha_0) = r\lambda \tag{2.43}$$

Now, on consider the two dimension space with one axis along 'b' the angle of incident and scattered along plane is β and β_0 respectively, then in order for constructive interference equation must satisfy.

$$b(cos\beta - cos\beta_0) = s\lambda \tag{2.44}$$

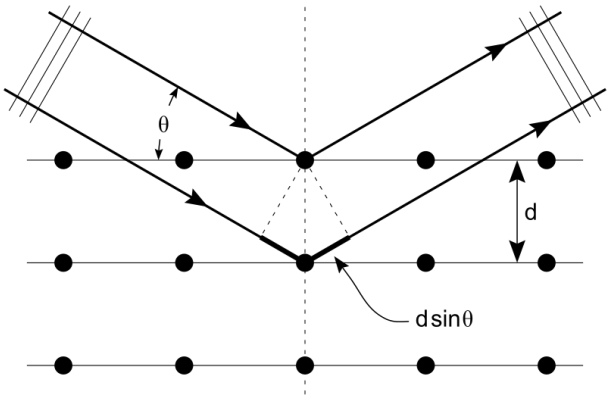

Figure 2.13: Bragg's law: two beams are incident on the crystalline solid at two different layers and scattered.There is a path difference between upper and lower beam.Lower beam cover the extra path $2dsin\theta$. [28]

2.4.2 Intensity in X-ray

The general formula of the intensity of diffracted X-rays for a powder crystalline sample can be find by combining the Debye-Waller and absorption coefficient factor given in the following equation [26].

$$I = |F|^2 p \left(\frac{1 + \cos^2 2\theta}{2 \sin^2 \theta \cos \theta} \right) \frac{1}{2\mu} (1 - e^{\frac{-2\mu t}{\sin \theta}}) e^{-2M_T} \tag{2.45}$$

Where :

F: Structure factor

p : Multiplicity factor

μ: linear absorption coefficient of the material

t: Sample thickness

M_T: Debye-Waller factor depends upon temperature

$\left(\frac{1+\cos^2 2\theta}{2 \sin^2 \theta \cos \theta} \right)$:Lorentz polarization factor

Lorentz polarization factor is the most is the most important experimental quality that control X-ray intensity with respect to diffraction angle [29].

2.5 DSC-TGA technique

2.5.1 Thermogravimetry

Thermal gravimetric analysis is a technique in which the mass of the sample is measured over time with varying temperatures. Using this technique, we can determine the physical properties phase transition, desorption and absorption, and chemical properties like thermal decomposition, chemisorption, and the solid-gas reaction of the sample material. In thermogravimetry, temperature, mass and time are the elementary measurements conducted by a gravimetric analyser which consists precise sample pan inside the furnace with a programmable control temperature. Generally, the temperature rises at a fixed rate to control the mass loss to retain thermal reactions. Sample can be heated under inert gas, CO2, N2 ambient air and oxidizing/reducing gases, and various pressures like high pressure, constant and control pressure [30].

Temperature increased at a constant rate for a known initial weight of the substance and changes in the weight are recorded as a function of temperature at different time interval. In thermo-gravimetry, the instrument used is a programmed precision balance for increased temperature called thermo-balance. In thermo-gravimetry, the instrument used is a programmed precision balance for an increase in temperature called thermo-balance.After collecting the data From thermal reaction collecting data is compiled into the plot with the percentage of initial mass along the y-axis versus temperature or time on the x-axis, referred to as the TGA curve.

2.5.2 Differential scanning calorimetry

Differential scanning calorimetry (DSC) is a thermoanalytical technique in which heat flow into or out of a sample is measured as the function of time or temperature while the sample is maintained at a controlled temperature. Generally, a DSC analysis temperature program is designed such that the sample holder temperature increase linearly as a function of time. DSC works on the basic principle that when a sample undergoes the phase transition, heat will require to flow through it to maintain the reference and sample temperature. The flow of heat to the sample depends on whether the process is endothermic or exothermic. For example, changing the sample phase from solid to liquid will require more heat to raise the temperature. This is because of the absorption of heat by the sample called the endothermic phase transition process. Similarly, some sample undergoes exothermic process like crystallization. Thus, observing the heat flow difference between a sample and reference DSC measures the heat absorbed or released during phase transition [31].

The results in DSC experiments are shown in the curve form of heat flux versus time or temperature. We considered two different conventions depending on the type of technology used in the experiment, like exothermic reactions in the sample showing the positive peak and endothermic for the negative peak.

2.5.3 TGA/DSC analysis

TGA and DSC are the combined temperature-based analytical technique. TGA measures a sample's mass variation when heated or cooled, while DSC measures how much energy a sample absorbs or releases during heating or cooling. Thermogravimetric analysis is often combined with other analytical methods like DSC (differential scanning calorimetry) because these two techniques together provide valuable information for the interpretation of the thermal analysis experiment. Using these two instruments temperature of different effects can be determined with great certainty. TGA/CGA is a unique tool for characterising materials' chemical and physical properties under controlled atmospheric conditions. Such measurements provide detailed information in multiple fields like minerals, pharmaceuticals, building materials, foodstuff, etc. A brief comparison of events and processes determined by TGA/DSC is given below.

Table 2.8: Comparison of TGA/DSC

TGA	**DSC**
Adsorption and desorption of gases	Melting behaviour
decomposition process	crystallization
Qualitative analysis	Curie temperature determination
Oxidation reactions	Glass transition
reactions and enthalpies	Heat capacity
Identification of decomposition	Reaction kinetics
Thermal stability	Phase diagram

Chapter 3

Experimental Details

3.1 In-situ Raman measurement

Raman spectra were obtained using a Renishaw InVia Raman spectrometer equipped with three laser sources and a Leica DM2700M microscope with objective $\times$ 50 were used. Here 633nm is the red wavelength produced from the He-Ne laser, and the other two, 532nm and 457nm, produce green and blue wavelengths, respectively, using a diode laser operating from 1 to 100 %. Power intensity. Magnification length, exposure time and laser power are working parameters that vary to obtain the best possible Raman spectra for various measurements. The first step involves using an instrument is calibration and alignment, taking silicon as reference material. Thus, the Raman spectra of silicon are measured, making us know whether our instrument is in the proper range to obtain an accurate measurement. Before taking all the measurements, we needed to close the door and switch off the lamp. All the acquisitions were made using WIRE software. After calibration and alignment of the spectrometer, measurements of the sample are performed utilizing the microscope at a suitable distance. Height and center vary according to the laser that we use. Sample can be seen on the computer screen by opening WIRE using a PC connected to

Figure 3.1: RENISHAW INVIA RAMAN MICROSCOPE at UiS lab

Raman spectroscopy.
Fix the spot on the sample by adjusting the calibration(changing the x, y and z-axis) or using a trackball.

In the measurement, we adjust the exposure time, laser power, magnification, temperature and intensity according to the material and laser we use. Usually, a blue laser is more intense/energy than a red or green laser. The sample was placed on the glass slide, and scans were taken for 10 s with 10 acquisitions per position. Once the scan was finished, the sample was moved vertically to another position, and the scan was repeated at five different positions. The reproducibility of the peak positions in all three scans indicates the sample's spatial homogeneity.

In first In-situ measurement, good Raman spectra of Ce-MOF-808 were obtained using 532nm laser with suitable working parameters. During measurements, if the spectra go out of the range (not good quality), fix it by varying the measuring parameters, significantly changing the intensity of the laser. The formic acid is liquid. Thus, use a glass tube for good spectra instead of a glass slide. Repeat all the experimental steps as applied in Ce-MOF-808 to find Raman spectra of trimesic acid, cerium ammonium nitrate and liquid formic acid are obtained under optimised conditions. To compare the spectra of Ce-MOF-808 with reference compounds trimesic acid as an organic linker, cerium ammonium nitrate as an inorganic precursor and formic acid as a modulator.

In the second Raman measurement, we analysis of the decomposition temperature of Ce-MOF-808 using a red laser. Standardized the apparatus taking silicon as reference material, then started calibration using optimized conditions. Working parameters include magnification power 50 $\times$, and intensity 100, acquisition time 10s with temperature interval 5$^{\circ}C$ per minute. Ramp up the temperature to 25$^{\circ}C$ and take the 1st Raman measurement. Next, evaluate the spectrum acquire in the first measurement and ramp up the temperature up to 100 $^{\circ}C$, take another measurement and compare it with the first one. Observe the Raman shift evaluating the measurement after every 50$^{\circ}C$ increasing temperature and continue measurements up to 22 $^{\circ}C$. If any spectra go out of the scale during the measurements, adjust it by varying the working parameters (intensity, magnification, acquisition time, and power). After 220 $^{\circ}C$, no further changes in the spectrum are observed; thus, evaluate the ex-situ measurement at room temperature.

In the third Insitu measurement, spectra of Ce-MOF-808 were evaluated using 532nm, 633nm and 457nm excitation wavelengths. Measuring parameters vary with varying laser wavelengths because of the energy differences. In-situ Raman measurement was acquired under optimized conditions, working three different lasers below.

Table 3.1: Optimized condition for three lasers

Laser	**Wavelength**	**Magnification**	**Intensity**	**Exposure time**
Blue	457nm	$\times 50$	10 %	10s
Green	532nm	$\times 50$	1%	60s
Red	633 nm	$\times 50$	50 %	1s

In the final Insitu Raman experiment, spectra of cerium MOF are obtained with a 532nm laser under multiple temperatures. A Raman band of silicon was used to calibrate the instrument. After calibration and standardisation, the instrument ramps the temperature from 25$^{\circ}C$ to 200 $^{\circ}C$ applying a temperature rate 5$^{\circ}C$ per minute. In order to determine MOF decomposition acquire Raman measurement after every 25$^{\circ}C$ until the temperature goes on 450$^{\circ}C$. With the further rise in temperature, no more spectra changes are observed. Thus ramp down from 100 $^{\circ}C$ to 25 $^{\circ}C$ and acquired the last measurement at 35$^{\circ}C$. To obtain precise spectra, adjust parameters using WIRE software connected with a PC during the experiment.

Data analysis

The measured data save in the desired file available in the .txt format, including measured values and relevant parameters. The WIRE software removes cosmic rays and subtracts the baseline from measured spectra. For processing data, extract the files using OriginPro 2019 software. In our experiment, we obtained Raman shift in terms of intensity. Plot data normalized intensity corresponding to Raman shift and then find characteristics feathers and peak analysis.

3.2 TGA-DSC

In order to compare the spectra of Ce-MOF-808 with Raman data, the combined TGA-DSC measurements were carried out using the TGA-DSC 3+ instrument from METTLER TOLEDO. Thermogravimetric analysis is frequently used to measure the sample mass over time with varying temperatures. Before using the sample for TGA analysis, grain the small amount of Ce-MOF-808 in powdered form using a mortar and pestle. For the decomposition of the Ce-MOF-808 alumina (Al_2O_3) crucible is used with 70 mul. TGA measurements were conducted in this experiment and ramp the temperature linearly with 5°C per minute. However, the Air (75% N_2 and 25% O_2) flow at the rate of 25 ml per minute throughout the experiment. A carrier gas flow throughout our experiment over the sample to protect the internals from corrosion and interact with sample gas-solid reactions. Sample heated with temperature changes linearly and measurements are taken to find the products released from the sample. At the same time, differential scanning calorimetry recorded the endothermic and exothermic processes during the sample decomposition.

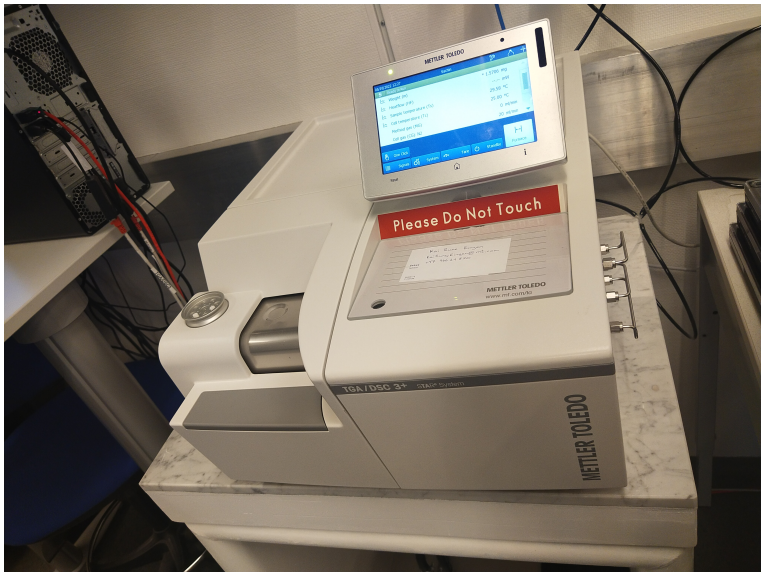

Figure 3.2: TGA-DCS 3+ METTLER TOLEDO situated at UiS laboratory

3.3 Powder X-ray

Using a copper X-ray source, the X-ray diffraction pattern of sample material analyzed by the D8 Advance diffractometer from Bruker in the Uis Materials' Science laboratory produces the wavelength (λ) 1.5418

Å. Before using the sample for powdered X-ray diffraction grain, the small amount of decomposed form of Ce-MOF-808 was obtained from TGA/DSC and pure Ce-MOF-808 in powdered form using mortar and pestle and spread on the silicon crystal sample holder in the form of a thin layer. Then, load the sample using DIFFRAC. SUITE software and place these samples in the two different flipstick positions of Bruker's D8 Advance diffractometer for XRD analysis.

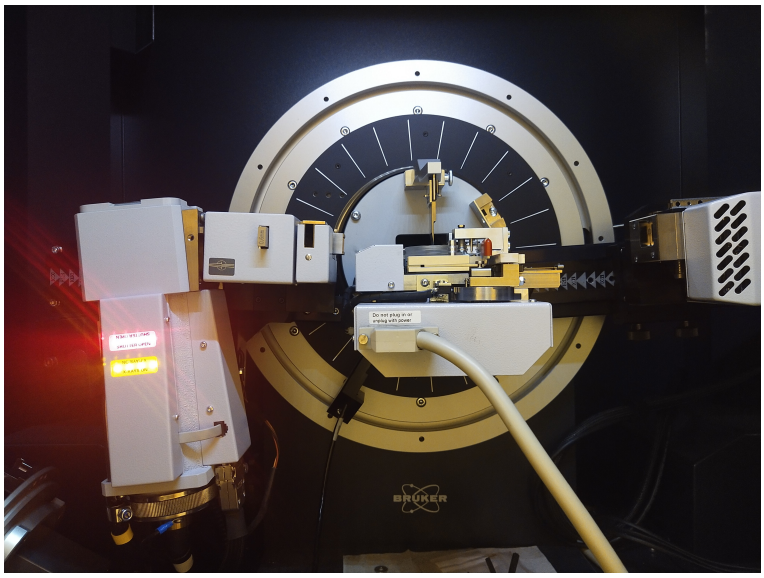

Figure 3.3: Bruker's D8 Advance diffractometer situated in the UiS Materials' Science lab

The essential elements in the D8 advance diffractometer are a sample holder, an X-ray detector and an X-ray tube. For this experiment, X-rays are generated by heating the filament in the cathode ray tube were accelerating by applying 40 Kv voltage with 25mA bombarded the target material with high energy electrons. When the fast-moving electrons have enough energy to knock out the inner electrons, the characteristics of X-ray spectra are produced that contain various components with Kα and Kβ are well known. Kα further splits up into two components, $K_\alpha 1$ and $K_\alpha 2$. Monochromatic X-rays produced by monochromatic crystals are necessary for diffraction. These monochromatic X-rays are focused onto the sample by selecting the specific range of angles between the X-ray source and the detector. The sample and detector are rotated with a specific range of rotations per minute; thus, spectra are recorded in a graph with scattered intensity along the y-axis and 2theta along the x-axis. $2theeta$ is the angle between the detector and the X-ray source. The diffractometer geometry is set so that the sample rotation is synchronized with incident X-rays which satisfies Bragg's law to produce constructive interference, and a peak pattern can be seen on the computer screen.

$$2d \sin\theta = n\lambda \tag{3.1}$$

2θ range along the x-axis is selected according to sample properties. For Ce-MOF-808 2θ range is selected from 10-90 degree.

3.4 Experimental and Computational details

R offer wide range of software packages which are being actively developed. The package corr2D contains a numerous functions like corr2d(), two plotting functions plot_corr3din3d() and plot_corr2d() for resulting correlation item. To get started user supplies data in the form of matrix [row× column] containing corr2d(). Input matrix contains: perturbation values, number of spectral values by columns. The column of the input matrix should contain the spectral value names, and rows can be included with the perturbation name. Our spectra are temperature-dependent Raman spectra; thus, the spectral variable v is the relative wave number. This section will look closely at the correlation function corr2d(), input perturbation variable, R script, generate dynamic spectra, etc. [1].

1. If the perturbation values are nearly equidistant, there is no need for interpolation, and reasonable results are acquired. However, in case of uneven distribution, there must be necessary the interpolate the perturbation values. In the case of corr2d(), various interpolation algorithms can be used. These lines of code show the interpolation process [1].
   R> TIME <- seq(min(Time), max(Time), length.out = N)
   R> tmp <- apply(Mat1, 2, function(y) Int(x = Time, y = y))
   R> Mat1 <- sapply(tmp, function(x) x(TIME))
   R> Time <- TIME

2. The second step in 2D correlation is to calculate the dynamic spectra constructed from the original dataset by subtracting a reference spectrum. In 2D correlation analysis, a perturbation means spectrum is chosen as the reference spectrum. If no reference spectrum is selected, the perturbation means spectrum is calculated from the input matrix Mat1, and the dynamic spectra become the mean-centred spectra. To convert dynamic spectra into mean spectra. To convert dynamic spectra into mean spectra [1].
   R> if (is.null(Ref1))
   + Ref1 <- colMeans(Mat1)
   + Ref2 <- colMeans(Mat2)
   +
   R> Mat1 <- sweep(Mat1, 2, Ref1, "-")
   R> if (Het == FALSE)
   + Mat2 <- Mat1
   + else
   + Mat2 <- sweep(Mat2, 2, Ref2, "-")
   +

3. Before doing correlation scaling, corr2d() scales the dynamic spectra. Then, the standard deviation auto-scaling can scale-out such mean dynamic spectra. m.n number of calculations are necessary to find auto-scaled dynamic spectra, where n is the number of spectral values within each spectrum and m is the number of spectra in our dataset. For synchronous and asynchronous spectrum, scaling will be [1].
   R> if (scaling > 0)
   + sd1 <- apply(Mat1, 1, sd)

```
+ sd2 <- apply(Mat2, 1, sd)
+ Mat1 <- Mat1 / (sd1^scaling)
+ Mat2 <- Mat2 / (sd2^scaling)
+
```

Chapter 4

Results and Discussion

4.1 Decomposition of cerium metal-organic framework

4.1.1 In-situ Raman measurements

The first part of the measurement was to obtain and assign Raman spectra of Ce-MOF-808 and the related compounds. This was done with three laser wavelength to ensure reproduciblity of the measurements and no sample damage with any of the laser. The figure 4.1 shows the Raman spectra of Ce-MOF-808 and its precursors obtained with 532nm laser. Formic acid was used in the synthesis and can remain as an impurity in pores. It is the simplest carboxylic acid with the formula HCOOH. Therefore, its Raman spectrum should contain the vibrations due to C=O, C-H, C-O, and OH. O-H stretching is expected above 3000 cm^{-1} outside of the range of the recorded spectrum. The assignment is summarized in Table 3.1. The peak at 2957 cm^{-1} is assigned to the C-H bond. The peak at 1397 cm^{-1} is attributed to the C-H wag, and 1663 cm^{-1} attributes to the C=O stretching mode. Besides, the peak of symmetric C-H stretching mode at 2769 cm^{-1} and bending located at 1204cm^{-1} has been assigned to the C-H mode, which shows the opposite Raman shift with the C=O bond group. Symmetry stretching and bending of the C-H bond occurs at 1061 cm^{-1}. At 1001 cm^{-1} spectrum peak is weak, showing the ring breath mode in which all C-C bonds of the ring contract and relax simultaneously [32][33]. In MOF materials, carbonyl modes are of particular importance because they are widely used to find the presence of residual acid. The C=O modes of aromatic acid appear at 1663 cm^{-1} because of the conjugation of the carboxyl group [34]

Consider the Raman spectra of trimesic acid in fig 3.1. Trimesic acid, also known as benzene 1,3,5 -tricarboxylic acid, contains a ring, -OH groups, and C=O groups. Trimesic acid is an organic linker in Ce-MOF-808. Raman vibration modes are O=C-O, C-O-H stretching vibration, benzene ring breathing vibration, symmetric stretching vibration of C=O, C-O-H asymmetric stretching vibration, O-C=O wagging vibration, COOH out-of-plane vibration, and C-C symmetric stretching mode [35]. The peak at 3085cm^{-1} is weak and assigned to -CH stretching, whereas at 1653 cm^{-1}, C=O stretching. The peak from 1426 to 1590 cm^{-1} is broad and weak and contains an aromatic ring. However, we can see there is a shoulder developed at 1252 cm^{-1} . The C-H out-of-plane bending vibrations are attributed to 950cm^{-1} and 906 cm^{-1} in Raman. The assignment of each peak can be seen in table 3.1. Symmetric O=C-O stretching modes at 735 cm^{-1} and an asymmetric twisting of some of the benzene rings and carboxyl groups at 787 cm^{-1} are also observed. Characteristics features are not shown in metal complexes which proves that carboxylate groups are involved in the coordination with metal. Bond strength in

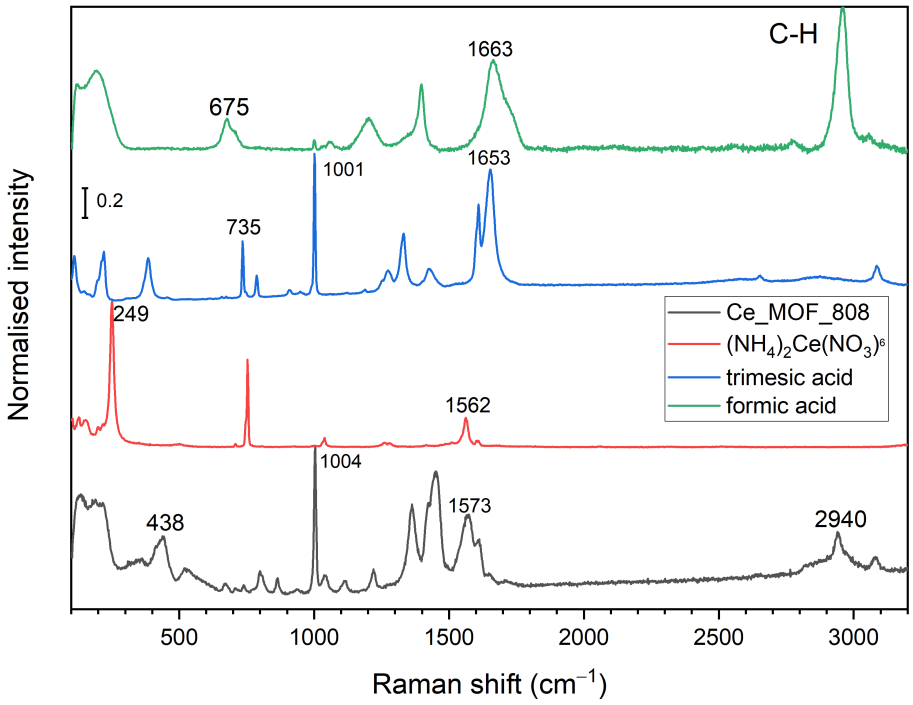

Figure 4.1: Raman spectra of Ce-MOF-808, precursors obtained with 532 nm laser: organic linker (trimesic acid), inorganic precursor (cerium ammonium nitrate), and modulator (formic acid, liquid).

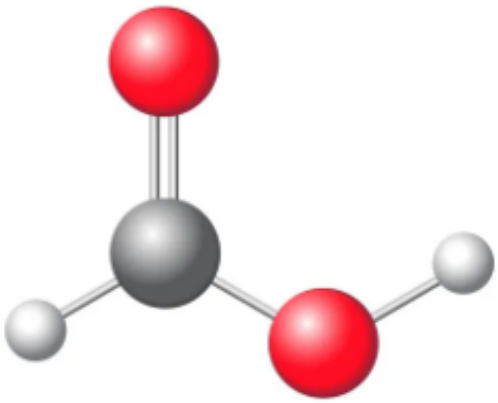

Figure 4.2: Structure of formic acid gray ball (C), red ball (O) and white ball (H) [36]

carboxylate groups is changed because of the replacement of acidic hydrogen with metal ion and loss of intermolecular hydrogen bonding; thus, distinct changes in Raman spectra of trimesates compared to trimesic acid. For example, Raman shift because carboxylic group vibrations disappear in complexes and peaks derived from carboxylate anion vibration [37].

Cerium ammonium nitrate is an inorganic precursor in Ce-MOF-808 with formula $(NH_4)_2Ce(NO_3)_6$. Raman modes in cericium ammonium nitrates are N=O stretching asymmetric and ONO bending. From 1260-1279 cm^{-1} Raman shift is very weak describes the NO stretching of asymmetric, whereas peak assign at 1040 cm^{-1} reveals the opposite behaviour $i.e.$ NO symmetric stretching mode. Raman data indicates there is possibility the two cerium atom bridging with oxygen in the acidic solution of cerium

Table 4.1: Peak assignments of observed Raman shifts for the spectra of Ce-MOF-808 and its precursors

Ce-808-MOF	$(NH_4)_2Ce(NO_3)_6$	**Trimesic Acid**	**Formic Acid**	**Assign Peaks**	**Ref.**
		3085 w		-CH stretching	[37]
3080 w				C-H stretching, aromatic	[32]
2940 m			2957 s	C-H stretching,aliphatic	[32]
1713 vw			1722 sh	uncoordinated -COOH	[38]
1647 vw		1653 s	1663 s	C=O stretching	[32]
1612 s				stretching mode -COOH	[39]
	1609w	1609 s		Anti-symmetric stretching C-O	[35]
1573 s				stretching mode -COOH	[39]
	1562m			bounded nitrate	[40]
1450 s				C-H bonding	[41]
1422 s				aromatic ring	[41]
		1426-1590w		Aromatic ring	[37]
			1397 s	C-H wagging	[32]
1363 s				stretching mode -COOH	[39]
			1347 sh	In plane bending CH	[33]
		1331m		CH twisting	[42]
	1260-1279 vw	1274 w		NO stretching asymmetric	[43]
		1252 sh		CO stretching	[42]
		1189 vw		OH twisting	[42]
1220 w			1204 m	CO stretching	[33]
1112 w				CO bending	[44]
	1040 vw			NO stretching symmetric	[43]
1036 w				CO bending	[38]
			1061 w	C-H bonding	[32]
1004 s		1001 s	1001 w	ring breathing mode	[35]
		950 vw		Out of Plane bending -OH	[42]
934 vw					
		906 vw		out of plane Bending -OH	[42]
866 w				O-H bending	[44]
800 m					[44]
		787 w		Carboxyl R-COOH	[35]
	753 s			ONO bending	[43]
739 w		735 m		symmetry stretching O=C-O	[35]
			710 sh	OCO in plane bending	[33]
706 w				CeO bond	[38]
670 w			675 m	OCO vibration	[32]
518 w,br				Carboxyl bonding	[44]
		383 m		symmetric stretching C-O-H	[35]
438 m				Ce-O stretching	[44]
344 br					
	249			lattice mode	[43]
217 s		220 m		benzene ring	[35]
			195 s	O-H-O stretching	[33]
180 s				symmetry vibration benzoate	[41]
s=strong	br=broad	vw=very weak	m=medium	sh=shoulder	

ammonium nitrate where each cerium is coordinated to oxygen atom.

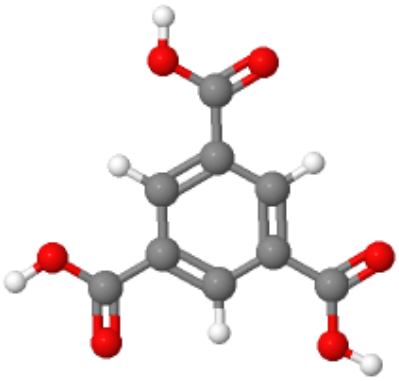

Figure 4.3: Trimesic acid red ball (O), white ball (H) and gray ball (C)[45]

Such coordination can be seen when the intense band at 249 cm^{-1} is assigned to the Ce-O-Ce lattice vibration mode. The weak bands of Raman shift at 1255 cm^{-1} and 1040 cm^{-1} can be assigned to bound nitrate. The incidence of the Ce-O-Ce Raman vibration in the presence of massive free nitrate in an acidic solution illustrates the stability of the oxide under conditions that should be unfavourable toward hydrolysis and favourable toward the hexanitrato monomeric anion [40]. The structure of cerium nitrate shown in the figure 4.4.

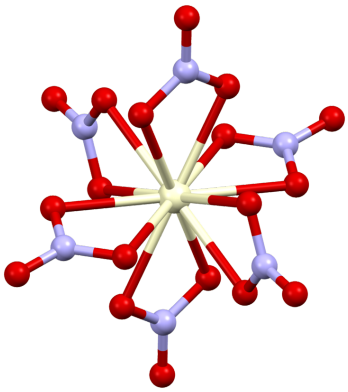

Figure 4.4: Cerium Nitrate White (Ce), Blue (N) and Red (O) [46]

Vibrational modes of the corresponding molecular groups' clusters can be expected. The Raman shift at 3080 cm^{-1} is weak, indicating the C-H stretching mode of vibration with aromatic hydrocarbons, while the peak at 2940 cm^{-1} is medium, showing a similar mode of vibration with aliphatic hydrocarbons. The Raman shift at 1713 cm^{-1} is very weak, corresponding to uncoordinated -COOH of free BTC (Benzene tricarboxylate) in MOF-808. There is a strong peak at 1450 cm^{-1} because of C-H bonding; however, at slightly left of this peak at 1422 cm^{-1}, the shoulder may be possible because of the aromatic ring.

From the spectra of cerium mof-808 it can be observe that there are several peaks from 500 cm^{-1} to 1400 cm^{-1}, while the peak at 1004 cm^{-1} is strong, indicating the ring breath mode of vibration. However the weak peaks at 1112 cm^{-1} and 1036 cm^{-1} can be assigned to the C-O bending vibration of Ce-OCH_3 and methoxy group on both sides of cerium respectively. The assignment of raman peak at 866 cm^{-1} is

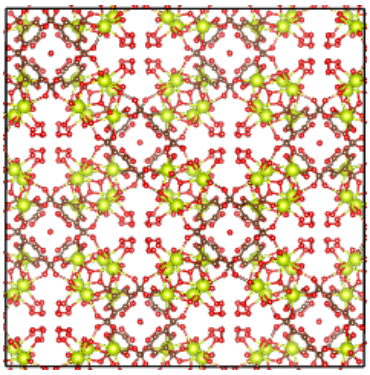

Figure 4.5: Ce-MOF-808 using VESTA software

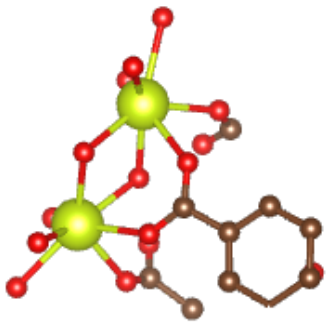

Figure 4.6: Ce-MOF-808 linkers using VESTA

weak is possible due to hydroxide ion. The stretching of Ce-O attribute to the raman shift at 438 cm^{-1} and near to this there is broaden peak contribition to the liberation mode of ammoniun cation. The broad and weak peaks from 438 cm^{-1} to 1220 cm^{-1} presented in raman spectra may be assigned due to grain or less crystallinity.

Ce-MOF-808 three laser

Fig.33 describes the comparison in the normalized Raman spectra of Ce-MOF-808 with red, green and blue laser were obtained using a Renishaw InVia Raman spectrometer. The peak intensity at 1002 cm^{-1} indicating the ring breathing mode which is more intense in green and red laser compare to the blue. However, on the contrary the Raman peak intensity at 2939 cm^{-1} assigned the C-H stretching aliphatic ring shows opposite behaviour. The spectra for the sample Ce-MOF-808 were collected using varying wavelength indicating change in the intensity of the peak at 443 cm^{-1} attribute Ce-O stretching maybe because of varying intensity of laser beam.

The Raman peak at 1449 cm $^{-1}$ assign the C-H bonding in the calculated spectrum is significantly stronger using laser with shorter wavelength then corresponding peak with longer wavelength. The possible reason may be because of structure sensitivity of material with laser intensity. Interestingly, the Ce-MOF-808 structure indicate inclined Raman-active peak around 70 cm^{-1} using red laser, which has not been found using green and red laser. This may possible because of the other two lasers are more intense compare to red laser.

In-situ Raman measurements of Ce-MOF-808 with 633 nm laser

The peak at 1001 cm^{-1} indicating the ring breathing mode of the linker progressively decreases in intensity with increasing temperature. A similar behavior is observed for the rest of the MOF peaks above 500 cm^{-1}. The relative intensities of the peaks at 1571-1608 cm^{-1} are reversed in the spectra at 50 and 220$^{\circ}C$ which may indicate that these peaks belong to different molecular groups. The intensity decrease in the peak at 800 cm^{-1} seems the slowest compared to the other peaks. After reaching 220$^{\circ}C$, the Raman detector was saturated, and it was not possible to observe further changes . After cooling down, the features in the Raman spectrum of the MOF partially regained intensities.

The spectral changes below 500 cm^{-1} are different from the rest of the spectrum. In particular, we observe that the peak at 438 cm^{-1} firstly decreases and above 175$^{\circ}C$ a new peak arises at 451 cm^{-1}.

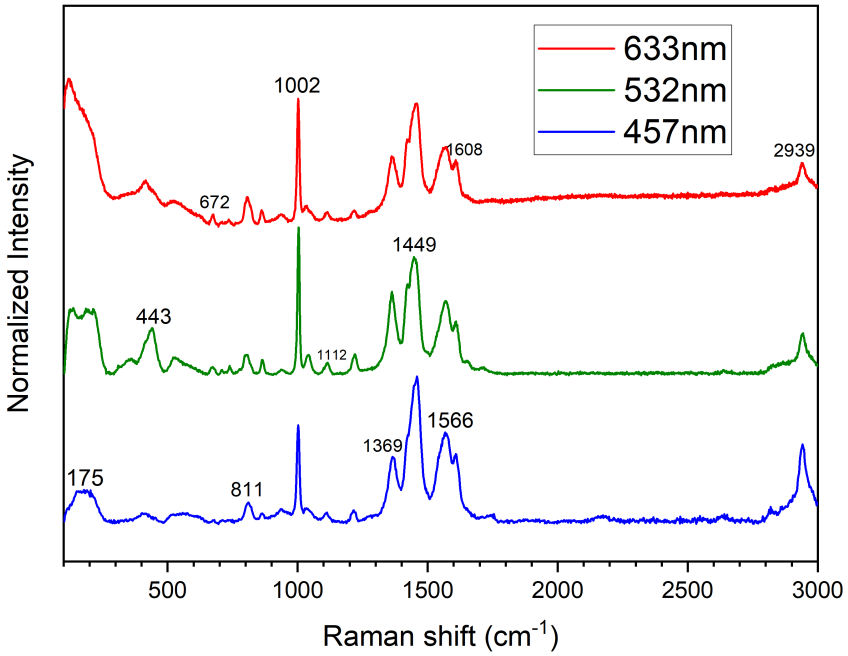

Figure 4.7: In-situ spectra of CeMOF 808 using green, blue and red laser

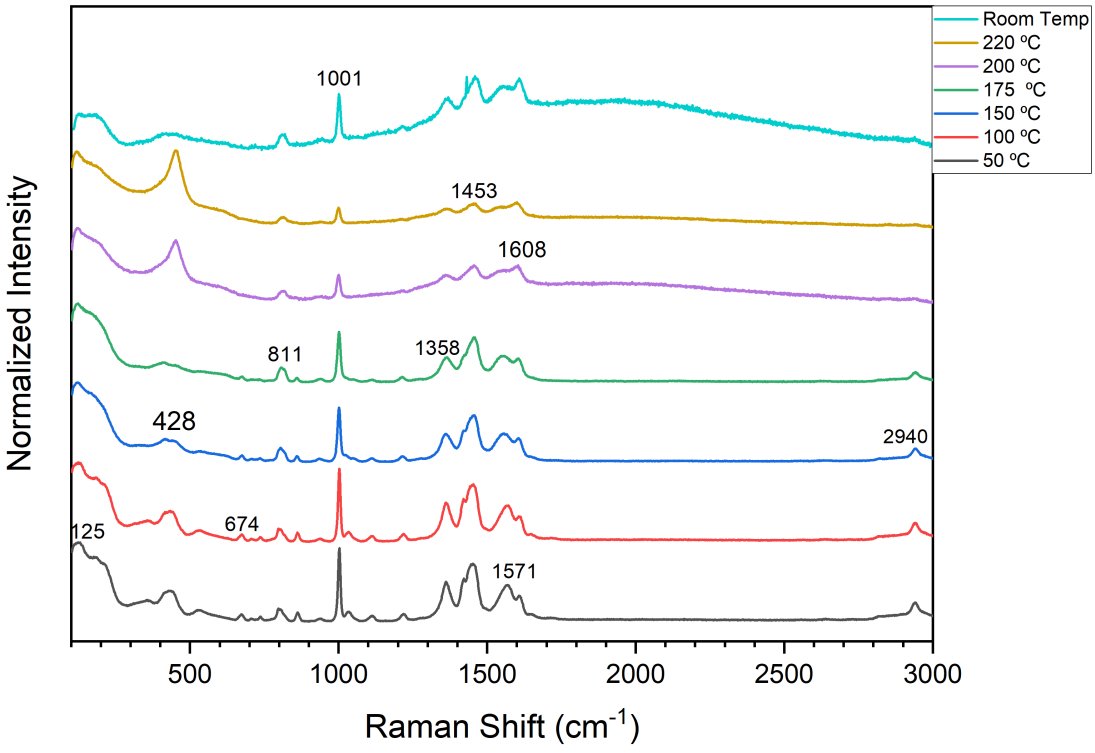

Figure 4.8: In-situ spectra with red laser

This peak disappears again when the sample is cooled to the room temperature after the experiment. The peak 2940 cm^{-1} is going off with increasing temperature until at 220°C no further peak can be seen. Raman shift at 1453 cm^{-1} developed the shoulder at 1422 cm^{-1} maybe because of aromatic ring which is invisible at high temperature 220°C.
On observing the in-situ raman spectra of Ce-MOF-808 using red laser, we can see variation in the raman peaks with temperature which shows there must be chemical transformation in MOF with varying temperature. The structure of Ce-MOFs transformed into ceria as calcination temperature increases. There are substituational variations in the structure of Ce-MOF as calcination temperature increase.

In-situ Raman measurements of Ce-MOF-808 with 5321 nm laser

In the fig 3.9 there is an In-situ raman spectra of CeMOF 808 using green laser variation in the temperature cause changes in the raman peaks. The particular chemical changes were explored by the Raman measurements within the pyrolysis temperature range from 200°C to 450°C , during which the crystalline phase in CeMOF changes significantly. From the graph it can be seen that for the Ce-MOF-808 there are more intense peaks towards the low raman shift. A clearly phase transition occur between 200°C and 300°C. As the temperature rises the structure of cerium MOF transfered into ceria. From 225°C no obvious peak were observed until temperature goes on 300°C which appears along with the characteristics peak of ceria at 500 cm^{-1}.

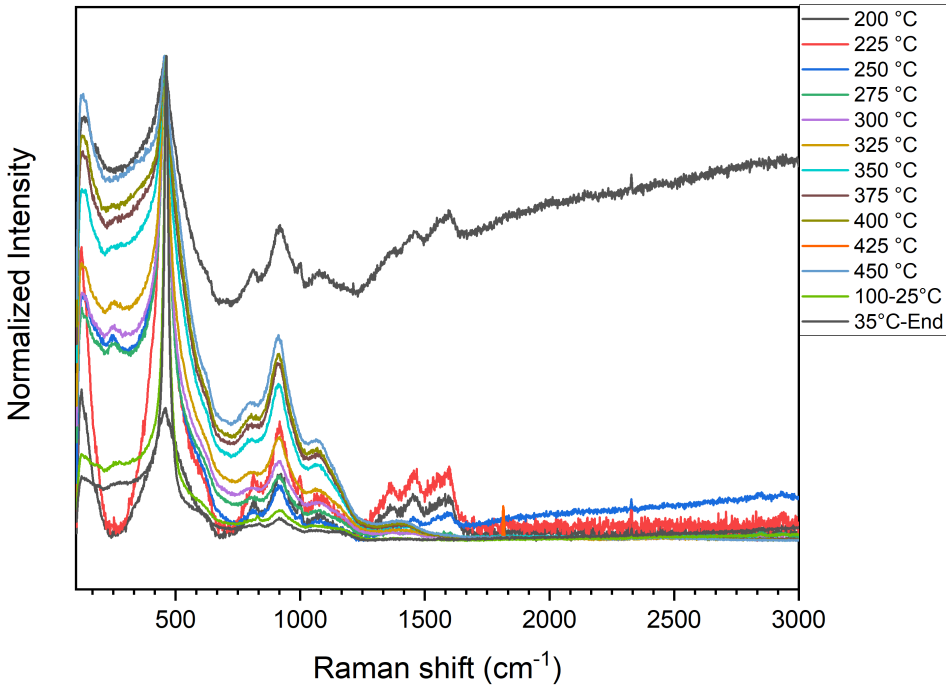

Figure 4.9: In-situ spectra of CeMOF 808 using green laser

A well crystallized ceria formed on rising the temperature to the higher level. According to the Raman analysis there is phase transition of Ce-MOF-808 at different temperatures. At the specific temperature Ce-MOF-808 retain its MOF structure. However at 250°C there is small changes in the structure of

the material and small particles are being formed which show burning of ligands cause the formation of smaller particles. At relatively low temperature cerium MOF maintained its structure because of coexistence of carbon framework and ceria, however with rising temperature carbon burned to carbon dioxide. [47]

At 460 cm^{-1} there is strongest vibrational raman peak attribute to the symmetric stretching vibrational mode in ceria. The decomposition temperature not only effects the grain size of Ce-MOF-808 but also the structural defects of the crystal. From 1700 to 3000 cm^{-1} there is smooth region and doesn't appears any peak in this region. Generally, the spectra of Ce-MOF-808 appears intensity of the Raman peaks proportional the temperature, however in some particular regions it behave opposite. Peak's strength in the region 1300 cm^{-1} to 1700 cm^{-1} increase from $200°C$ to $250°C$, while its decline from $300°C$ to $450°C$ temperature.

4.1.2 Powder X-ray diffraction analysis

In this experiment, Ce-MOF-808 and decomposed form of Cerium MOF characterized by the powdered X-ray diffraction carried out in the D8 Advance Diffractometer situated in UiS Materials' Science laboratory. The X-ray diffraction (XRD) patterns of the samples were obtained using Cu-Kα radiation of wavelength (λ) 1.5418 A. After extracting data using DIFFRACT.SUITE software, the data plotting was done completely in the OriginPro 2019 in the range of 10-90° at room temperature.

Decomposed cerium MOF

In thermogavometric analysis cerium MOF decomposed at 330° and acquired stabilization after completely changing Ce-MOF into CeO_2. The decomposed form further analyzed in powdered X-ray diffraction. X-ray powder diffraction was utilized to measure the structural properties of materials. The diffraction pattern of pure CeO_2 shown in fig. 4.10. The excellence peaks (111), (200), (220), (311), (222), (400), (331), (420) and (422) were obtained for their corresponding angle 28.56°, 32.73°, 46.97°, ^{5}5.71∘, 58.42°, 68.60°, 75.77°, 78.11°, 87.29° which confirm the formation of nanosized CeO_2 particles. Absence of impurity shows that pure CeO_2 synthesis from thermogravometry. Thus the average crystallize size D of sample can be calculated by Debye-Scherer equation given below [48].

$$D = \frac{k\lambda}{\beta cos\theta} \tag{4.1}$$

In the above equation D is the crystallize size, k is constant with take value 0.9 , λ is the wavelength of the Cu-kα radiation, θ is the diffraction angle and β is full width half maximum.

A comparison of CeO_2 with Raman spectra, there a sharp peak has been observed at 465 cm^{-1} assigned to the symmetric Ce-O vibration in CeO_2 lattice. Comparing the spectra obtained powdered CeO_2 peaks with Raman, it has been observed that peaks at oxide layer apperas broader as well as being shifted to lower wave numbers. In $Ce0_2$ the triply degenerate stretching vibration of the CeO_2 vibrational is due to the movement of the oxygen atoms. As the oxygen vacancy concentration increases, the mode of vibrations shift to lower frequency, broadens peaks and becomes asymmetric. The oxidation of cerium in air shown increase in the CeO_2 layer confirmed by XRD and Raman spectroscopy. The table below shows the Miller indices corresponding to their peaks with angle 2θ.

We have already detailed analyze Ce-MOF-808 and its precursors using Raman spectroscopy with red and green laser at different temperature. Now, the structure of same MOF characterizes by powdered

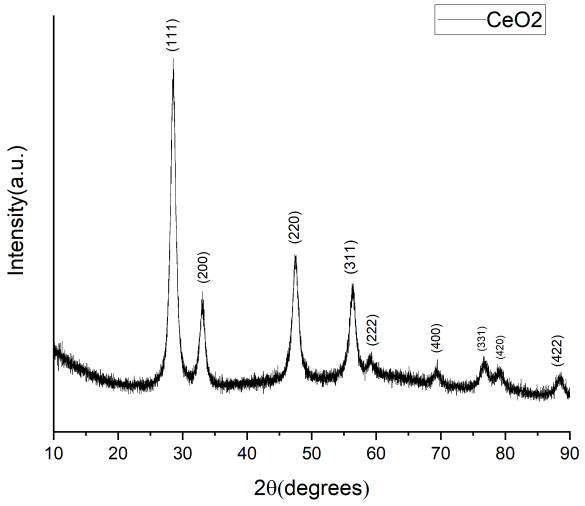

Figure 4.10: XRD pattern of decomposed cerium MOF

Table 4.2: Miller indices corresponding to peaks and angle 2θ.

(No.)	(hkl)	2θ	**d**
1	(111)	28.24	3.15
2	(200)	32.73	2.73
3	(220)	46.97	1.93
4	(311)	55.71	1.64
5	(222)	58.42	1.57
6	(400)	68.60	1.36
7	(331)	75.77	1.22
8	(420)	78.11	1.11
9	(422)	87.29	1.05

x-ray diffraction at room temperature. Fig. 4.10 shows the x-ray diffraction pattern of the cerium-based MOFs carried out in D8 advanced diffractometer.

X-ray diffraction pattern of Ce-MOF-808 display its diffraction peaks at 2θ =4.52°, 8.52°, 17.36°, 20.39°, 24.27°, 28.53° and 38.46° with Miller indices are (111), (222), (551), (822), (771), (866) and (999) respectively are strongly supported by the literature [49]. These XRD peaks labeled with Miller indices using VESTA software. In addition to these peaks there are numerous miscellaneous peaks are also observed, which indicates sample has low crystallinity. However, XRD pattern in our experiment confirm that the our sample is precisely the target material without changing its crystal growth [49].

4.1.3 TGA-DSC measurement

In this experiment the decomposition of Ce-MOF-808 were performed using the combined differential scanning calorimetry-thermogravimetric analysis (DSC-TGA) instrument from METTLER TOLEDO. Sample is heated from $25°C$ to $500°C$ with constant heating rate 5k/min and Air (75% N2 and 25% O2) flow at the rate of 25 ml per minute throughout the experiment. The focal point of our experiment is to observe the heat flow and % of weight loss with temperature variation. Furthermore, to compare TGA curve analysis with already acquired results from Raman spectroscopy. Thermogravimetric analysis (TGA)

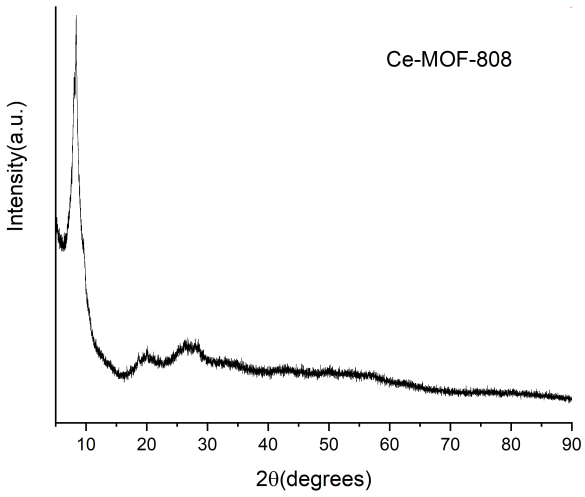

Figure 4.11: XRD pattern of Ce-MOF-808

experiment was carried out by heating the sample from room temperate to $500°C$ under air atmosphere with flow rate 5k/min. In the fig. below red line exhibit the thermogravimetric curve of Ce-MOF-808 which indicates the percentage of mass loss with decomposition temperature.

Ce-MOF-808 exhibited the weight loss linearly with rising temperature from $25°C$ to $250°C$. During the temperature interval $250°C$ to $310°C$, there is increasing the slop which indicates there is more weight loss with rising temperature. Ce-MOF-808 weight loss between room temperature and $310°C$ maybe due to high amounts of desorption of water and other impurities from the pores of the sample. However in the second stage weight loss occurs between $310°C$ to $330°C$ drastically, where benzene-tri-carboxilic acid transformed into carbonates and cerium MOF into cerium oxide. With temperature range from $330°C$ to $350°C$ there constant weight loss with increasing temperature. Alongside, in the final stage organic ligands and metal ion become individuals at $350°C$ to $500°C$, and both are gradually stabilized. Thus overall there is 52% reduction in the weight loss in TGA experiment [49].

In the fig. 44.11 black line exhibit the differential scanning calorimetry analysis of Ce-MOF-808 which indicates the heat flow through the sample with temperature variation. With temperature range from $25°C$ to $250°C$ there is vertical line (zero slop) which indicates that no variation in heat flow with rising temperature. This behaviour exhibit the stability of sample until $250°C$. There is rapid increase in the heat flow from $250°C$ to $310°C$ and endothermic process takes place, indicates the decomposition of cerium MOF into cerium oxide. In contrast, there is opposite behaviour i.e abrupt decrease in the heat flow and exothermic process takes place until $375°C$. Further rising the temperature no heat flow, indicate that decomposition has been takes place and sample is stabilized.

Three small plots above TGA-DSC analysis in fig. 4.11 are acquired from Raman spectroscopy using red and green laser. A small plot "a" above the right corner of fig. 4.11 acquired from the red laser within temperature range $25°C$ to $250°C$. With increasing temperature the peak strength at 518cm^{-1} attribute to carboxyl bonding become broader. Plot "b" indicates the variation in Raman spectra within the temperature range $250°C$ to $400°C$ was obtained using green laser. Comparing to these spectra with DSC analysis a distinctive variation in the heat flow can be observed i.e the weight loss decrease fastly

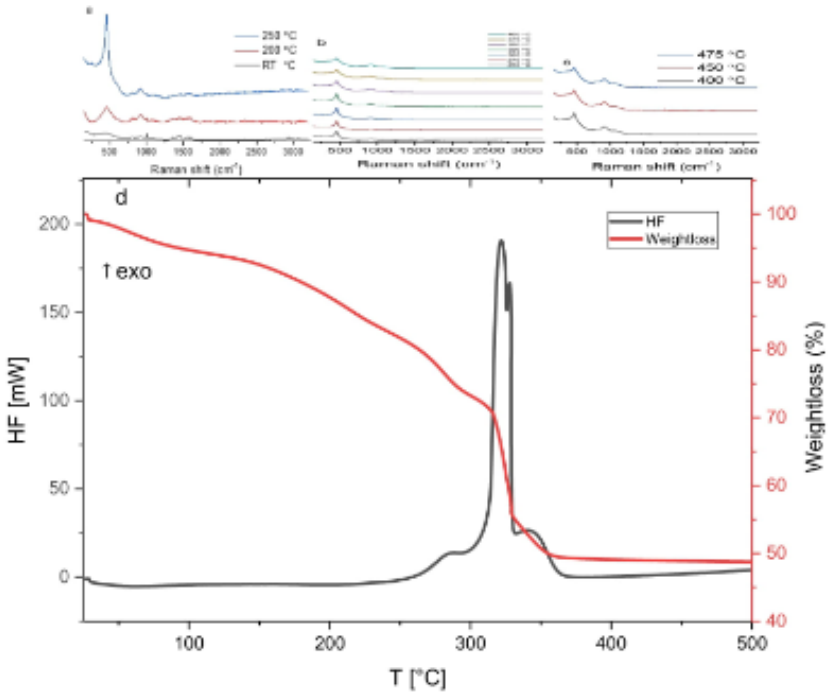

Figure 4.12: The graph shows the % weight loss as well as heat flow with varying temperature

and decomposition takes place. In contrast to plot "b" heat flow and weight loss from $400°C$ to $475°C$ approximately constant.

4.1.4 2D correlation analysis of Raman data

Nowadays generalized 2D correlation spectroscopy, gaining well known method applicable extensively analysis of various spectral data. Applying two-dimensional correlation technique can sort out the valuable information in systematic changes of analytical signals observed under the applied external perturbation. In 2D correlation, the external perturbation in the sample material induced the variation in the spectra which can be analyzed by the auto as well as cross correlation. Such approach applied to understand the complex systems like MOFs, because 2D correlation provides distinctive information which is not detectable with conventional spectroscopic measurements [50].

Temperature induced variation of spectra has been studied for numerous system. Generally, such measurements are simple and straightforward that doesn't require any special equipment. It needs only temperature control instrument to maintain sample temperature during measurement. Thus, thermally induced spectroscopy is becoming attractive technique in 2D spectroscopy field [8].

2D corr plot

We measured in situ Raman spectra of Ce-MOF-808 between $50°C$ and $220°C$ using red laser. We analyzed firstly in situ Raman spectra of Ce-MOF-808 at various temperature in Raman experiment. There are three auto peaks at 1358, 1453 and 1571 cm^{-1} were observed in the synchronous 2D correlation spectrum as shown in Figure 4.10. Auto peaks are appearing at the diagonal positions of synchronous 2D spectrum indicates the spectral intensity changes for these Raman bands during the temperature

variation.The auto-peaks at 1458, 1571cm^{-1} was observed attributed to the stretching vibration of carboxylic acid. In addition to this a prominent peak appears at 1453cm^{-1} attibute to the -CH bonding. Thus, the strong autopeaks shows the strong variation in the in intensity under perturbation. Auto peaks are always positive and seen only in the synchronous 2D correlation spectra. Cross peaks are appearing above

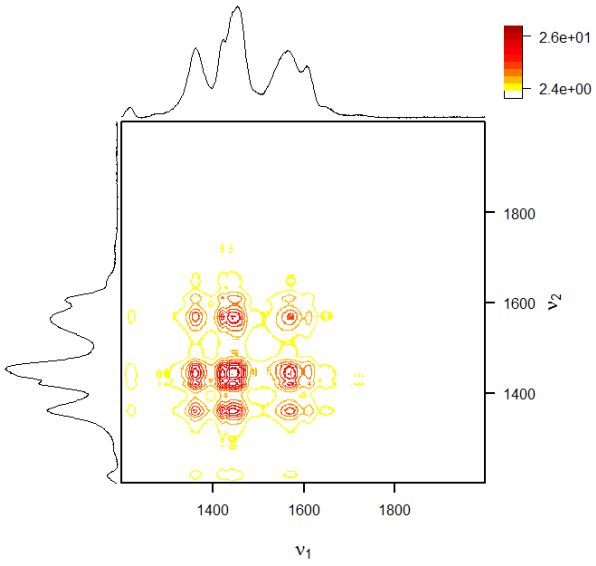

Figure 4.13: Synchronous 2D correlation spectrum of Ce-MOF-808 obtained using red laser

and below the diagonal positions of two-dimensional spectra. There are positive as well as negative cross peaks as shown in the table below. The presence of negative cross peaks (1358, 1455) and (1453, 1571) cm^{-1} consistent with the fact that intensity of one organic molecule increase while other is decreasing as MOF is heated. In other words some of the ordered crystalline structure change it phase. However there are also positive cross peaks has been observed at (1358, 1571)cm^{-1} in synchronous 2D correlation spectra which confirmed that intensities of organic molecule move in the same direction i.e both are increasing or decreasing. As the synchronous spectra is symmetric spectrum with respect to diagonal, so they appears both diagonal and off-diagonal positions. In synchronous spectra all the peak signs have been shown in the table below. The 2D asynchronous spectra can support to evaluate the sequential order

Table 4.3: Signs of peaks in synchronous spectra

	1358	1453	1571
1358	+	-	+
1453	-	+	-
1571	+	-	+

of specific events along external perturbations. As asynchronous correlation spectra is anti-symmetric, so there are no auto correlation peaks developed on the diagonal positions. However in asynchronous 2D correlation Raman spectrum several cross peaks appears on the off-diagonal positions as shown in fig. 4.11. These cross correlation peaks maybe positive or negative depends the intensity variation. The band near 1440 cm^{-1} split into two separate bands located around 1438 and 1453 cm^{-1};likewise the band near 1570 cm^{-1} split up into 1571 and 1568 cm^{-1}. The signs of asynchronous cross peaks indicate that there is decrease in intensities at 1453 and 1571 cm^{-1} occur at higher temperature as compared to rapid

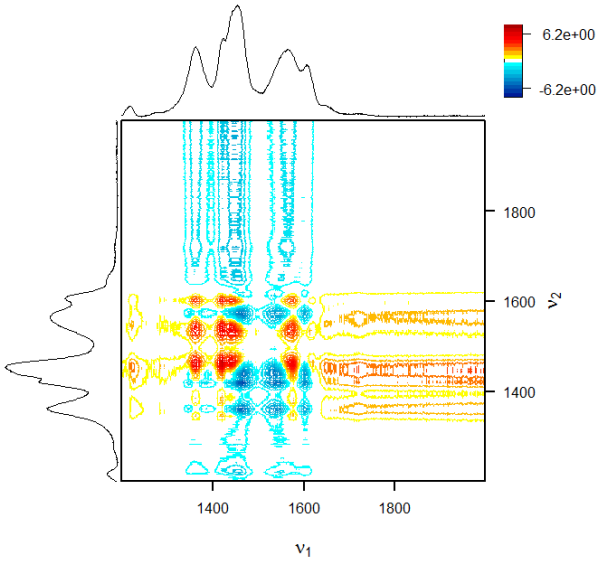

Figure 4.14: Asynchronous 2D correlation spectrum of Ce-MOF-808 obtained using red laser

decrease at 1438 and 1468 cm^{-1}. In asynchronous spectra, the positive crosspeaks at 1438cm^{-1} maybe because of aromatic ring, while negative crosspeak appeared at 1600cm^{-1} exhibit the anti-symmetric stretching behaviour. Some of the cross peaks in asynchronous spectra appeared associated with noise. such appearance means that the intensity of a band corresponded distorted maybe because of cosmic or some background radiation. In asynchronous spectra variation in the signs suggest there is chemical transformation in the the MOF with temperature. The cross-peaks of every two bands are shown in the asynchronous map fig. 4.11 and their signs are given in the table below. In the asynchronous map, the red represents a positive sign, while the blue represents a negative sign.

Table 4.4: Sing of peaks in asynchronous spectra

	1358	**1438**	**1453**	**1571**	**1600**
1358	0	0	+	+	+
1438	0	0	+	+	+
1453	-	-	0	-	0
1571	-	-	+	0	+
1600	-	-	0	-	0

Using Green laser

In the first experiment we analyzed in situ Raman spectra of Ce-MOF-808 using red laser with temperature range $50°C$ and $220°C$. Further increase in temperature cause the noise and distortion in the spectra using the same laser. To acquire the good spectra of Ce-MOF-808 at high temperature replace the red laser by green laser. Thus, we measured in situ Raman spectra Ce-MOF-808 in temperature range $200°C$ and $450°C$ using green laser. In synchronous 2D correlation spectra three auto peaks were observed at 438, 866 and 1363 cm^{-1} appears at diagonal positions of synchronous 2D correlation spectra shown in fig 4.12. These auto correlation peaks indicates the strong variation in the intensity under temperature variation. As the synchronous spectra is symmetric spectrum with respect to diagonal, so they appears

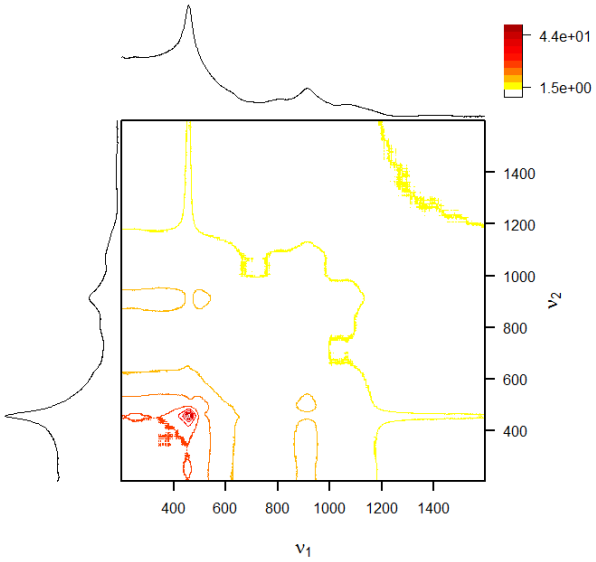

Figure 4.15: Synchronous 2D correlation spectrum of Ce-MOF-808 obtained using green laser

both diagonal and off-diagonal positions. Three main autopeaks 438, 866, 1363 cm^{-1} were displayed in the main spectra and their cross-peaks all exhibited negative signs, suggesting the intensity of these bands changes in the same direction. Peaks assignments to these 438, 866, 1363 cm^{-1} band spectra are Ce-O stretching, O-H bending and Ce-O asymmetric stretching respectively. In synchronous spectra all the peak signs have been shown in the table below. In asynchronous 2D correlation Raman spectrum cross

Table 4.5: Sign of peaks in synchronous spectra

	438	866	1363
438	+	-	-
866	-	+	0
1363	-	0	+

peaks appears on the off-diagonal positions as shown in fig. 4.11. These cross correlation peaks maybe positive or negative depends the intensity variation. The band near 400 cm^{-1} split into two separate bands located around 344 and 570 cm^{-1}. In asynchronous map, the band centred at 440 cm^{-1} was divided into two bands at 438cm^{-1} and cm^{-1}, and a series of series of cross-peaks correlated to 866cm^{-1} was observed, which is likely to be overlapped by the band at 438 cm^{-1} in the synchronous spectra. The bands were attributed at 344cm^{-1} was assigned to Cerium oxide stretching and the band at 570 cm^{-1} 0-C-O vibration.

The cross-peaks of every two bands are shown in the asynchronous map fig. 4.11 and their signs are given in the table below. In the asynchronous map, the red represents a positive sign, while the blue represents negative sign.

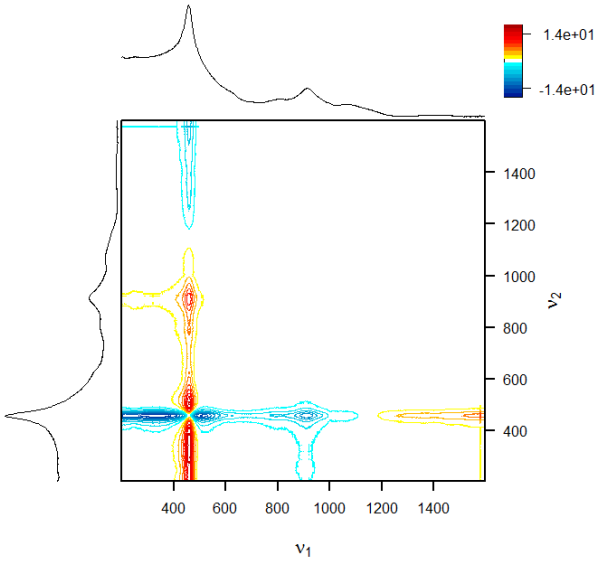

Figure 4.16: Asynchronous 2D correlation spectrum of Ce-MOF-808 obtained using green laser

Table 4.6: Sign of peaks in asynchronous spectra

	344	438	570	866
344	0	-	0	0
438	+	0	+	+
570	0	-	0	0
866	0	-	0	0

4.2 Magnesium Borohydride

4.2.1 Assignment of B-H and B-D modes

In-situ Raman data of $Mg(BH_4)_2$ has been studied at 140 °C by measuring the 20 spectra with 5 minutes each interval. There is a distinct Raman shift can be observe at 2320 cm^{-1} attributes the symmetric stretching of BH_4. Moving from lower to higher frequency, strength of the peaks going to increase, however there is an opposite behaviour in the lower frequency region. Multiple weak peaks developed in the 1600-1100 cm^{-1} region due to the transformation of BH_4 into bending mode of various newly formed of isotopes. The region 1500-2750 cm^{-1} developed multiple medium peaks due to stretching modes of vibration. With growing intensity at 1717 cm^{-1}, there developed shoulders at 1677, 1647 and 1606 cm^{-1}, which attributes to the symmetric B-D stretching in $BD_2H_2^{-1}$, BD_3H^{-1} and BD_4^{-1} respectively [5]. Equation 2.25 describes the Redlich-Teller product isotopic rule and there is also calculating the shift for A1 mode of BD4 with respect to BH4 using 2.33. Thus using this rule we can predict the peak position in the isotopic exchange of $Mg(BH_4)_2$. However there is an extensive variations in the peak position complicate the data analysis.

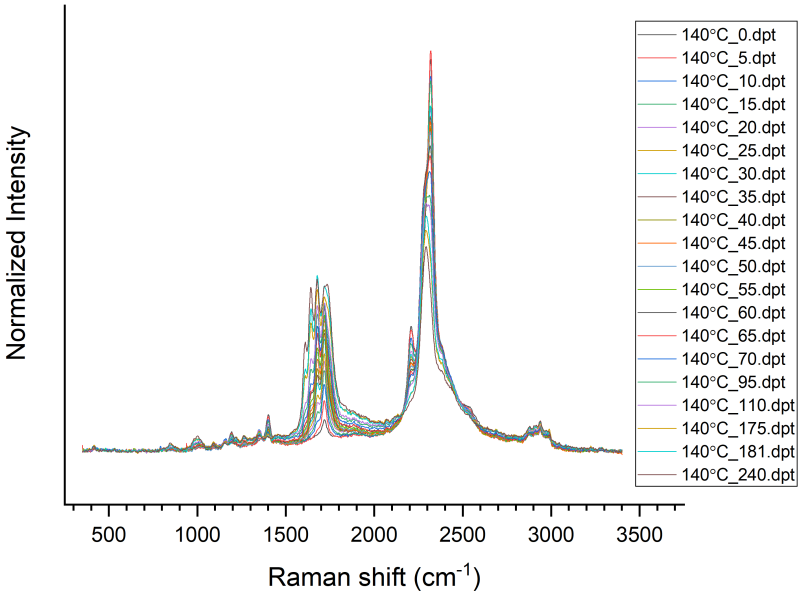

Figure 4.17: In-situ Raman data of $Mg(BH_4)_2$ at 140 °C

4.2.2 Raman data

Time-dependent Raman experiments are ubiquitous, which appears in many dynamic studies of chemical system. Main advantage of fast data collection is that a time-dependent perturbation can monitoring the several functional groups observable by Raman. 2D correlation analysis can enhance the spectral changes and simplification of complex spectral peaks [8]. Herein, we try to examine the 2D correlation analysis of already measured In-situ Raman data of $Mg(BH_4)_2$. A total of 20 spectra were collected with time interval 5 minutes of each spectra. Figure 4.17 is the generalized 2D correlation Raman spectrum corresponding to In-situ Raman data shown in Fig. 4.19. A synchronous spectra contain auto as well as cross peaks. Auto peaks appearing at diagonal positions of 2D correlation spectrum exhibit the spectral intensity changes for Raman bands during the observation period. The synchronous maps reveals the the two prominent peaks at 1717 and 2320 cm^{-1}. In addition to these three small but not obvious autopeaks were observed at 1606, 16047 and 1677cm^{-1} because of grew in intensity at 1717 cm^{-1} developed the shoulder at these points, which was attributed to the symmetric B-D stretching in BD_4^{-1}, BD_3H^{-1} and BD_2H^{-1} respectively. Besides these autopeaks there is distinctive crosspeak can be seen at 2320 cm^{-1} in distorted form indicating the destruction of BH_4^{-1} group. There is a small cross peak at 2200 cm^{-1} due to shoulder developing at 2320cm $^{-1}$. As synchronous spectra is symmetric spectrum with respect to

Table 4.7: Sign of peaks in synchronous spectra

	1717	2200	2320
1717	+	-	-
2200	-	+	0
2320	-	0	+

the diagonal, so they appears both diagonal and off-diagonal positions. In the synchronous spectra all the

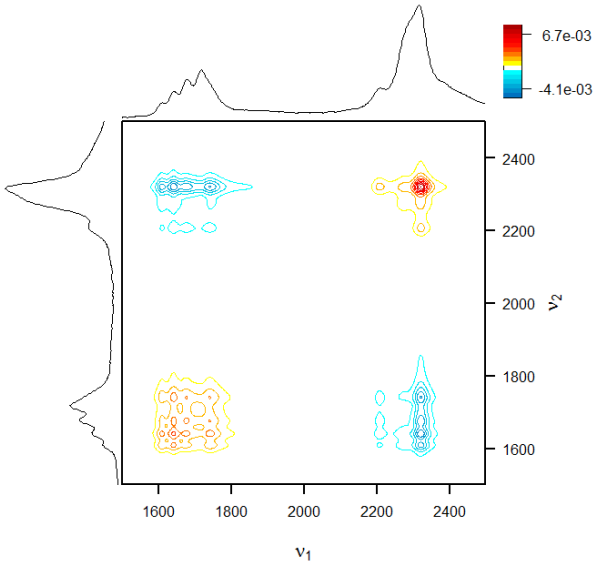

Figure 4.18: synchronous spectra of $Mg(BH_4)_2$

peak signs have been shown in the table below. As the synchronous spectra is symmetric, so the signs above and below the diagonal will be the same.

The asynchronous 2D Raman correlation spectrum provides a clear picture of the time-dependent variations of Raman intensities of component bands of $Mg(BH_4)_2$. It is obvious from the spectrum

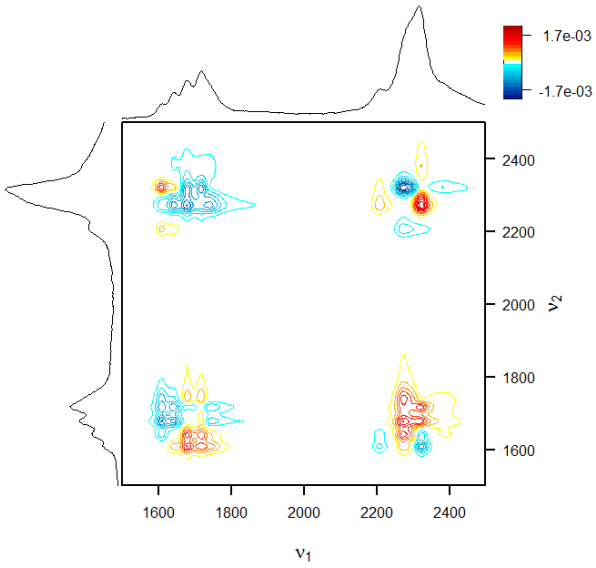

Figure 4.19: Asynchronous spectra of $Mg(BH_4)_2$

in figure 4.19. that asynchronous cross peaks are always developed between the pairs of Raman bands assignable to different species. The sequence of the events that happen during the experiment can be identified by the signs of asynchronous cross peaks. Some of the cross peaks are shaded are some of them are not. In asynchronous spectra shaded region indicates that time-dependent changes at v_1 occur after v_2. However the region without shaded behave opposite. From the figure 4.19. it can be seen that

asynchronous cross peak at coordinates 2275 and 2320 cm^{-1} is shaded. Thus the intensity change at 2275 cm^{-1} occurs after the change in 2320 cm^{-1}.

In asynchronous map, the band centred at 2300 cm^{-1} was divided into two bands at 2270 and 2320 cm^{-1}, and a series of cross peaks correlated to 1700 cm^{-1} was observed. The bands were attributed as follows: the band at 1717 cm^{-1} correspond to B-D stretching, and band at 2320 cm^{-1} attributes destruction of BH_4^{-1} group. In asynchronous map, red regions represent the positive sign while blue regions represent the negative sign. According to Noda rules by changing the spectral regions there is changing the spectral intensity.

Table 4.8: Sign of peaks in asynchronous spectra

	1606	1700	1717	2200	2320
1606	0	-	0	+	+
1700	+	0	+	0	-
1717	-	-	0	-	-
2200	-	0	0	0	+
2320	-	+	0	-	0

4.2.3 Conclusions

The aim of this thesis was to study the two-dimensional correlation analysis and apply it to two systems with different perturbation: time in $Mg(BH_4)_2$ and temperature in Ce-MOF-808. Herein, the spectroscopic technique utilized with Raman spectroscopy yielding valuable information about $Mg(BH_4)_2$ and Ce-M0F-808 by employing the temperature and time dependent perturbation to induce the spectral variations. In correlation technique synchronous as well as asynchronous maps were plotted using R language. These maps were used to determine the sequence of events happening during the experiment and to analyze the spectral features more clearly.

Raman spectra of Ce-MOF-808 were obtained using red laser with increasing temperature from 25°C to 220°C and for the green laser spectra acquired from 200°C to 450°C. The reason for characterization of sample material using different laser was used for optimization measurements conditions for Raman. In-situ raman spectra of Ce-MOF-808 using red laser, variation in the Raman peaks with temperature can be observe which shows there must be chemical transformation in MOF with varying temperature. After reaching 220 °C , the Raman detector was saturated, and it was not possible to observe further changes using red laser. Thus green laser used to find the particular crystalline changes in the Ce-MOF-808 within the pyrolysis temperature range from 200°C to 450°C. The peak intensity at 1002 cm^{-1} indicating the ring breathing mode which is more intense in green and red laser compare to the blue. However, on the contrary the raman peak at 2939 cm^{-1} assigned the C-H stretching aliphatic ring shows opposite behaviour.

A combined TGA-DSC instrument was used to heat the sample from 25°C upto 500°C to study the weight loss during the decomposition. There is rapid increase in the heat flow from 250°C to 310°C and endothermic process takes place, indicates the decomposition of cerium MOF into cerium oxide. This decomposed sample was then studied by using PXD techniques to check whether any crystalline compound is present. Comparing the spectra obtained powdered CeO_2 peaks with Raman, it has been observed that peaks at oxide layer apperas broader as well as being shifted to lower wave numbers.

In synchronous maps of $Mg(BH_4)_2$ two prominent auto peaks were observed at 1717 cm^{-1} and 2320 cm^{-1} attributes to B-D stretching and symmetric stretching of BH_4^{-1}. In asynchronous map, the band centred at 2300 cm^{-1} was divided into two bands at 2270 and 2320 cm^{-1} and a series of cros peaks correlated to 1700 cm^{-1} observed. The sequence of the events happening during experiment can be identified by the signs of asynchronous cross peaks. From the asynchronous map of $Mg(BH_4)_2$ the shaded region observe at coordinates 2275 and 2320 cm^{-1} which indicates the intensity change at 2320 cm^{-1} occur before 2275 cm^{-1}.

Bibliography

[1] R. Geitner, R. Fritzsch, J. Popp, and T. W. Bocklitz, "corr2d-implementation of two-dimensional correlation analysis in r," *arXiv preprint arXiv:1808.00685*, 2018.

[2] I. Noda and Y. Ozaki, *Two-dimensional correlation spectroscopy: applications in vibrational and optical spectroscopy*. John Wiley & Sons, 2005.

[3] K. Murayama, B. Czarnik-Matusewicz, Y. Wu, R. Tsenkova, and Y. Ozaki, "Chemometrics and two-dimensional correlation spectroscopy in the analysis of near-infrared spectra of protein," in *AIP Conference Proceedings*, vol. 503, no. 1. American Institute of Physics, 2000, pp. 183–196.

[4] S.-i. Morita, Y. F. Miura, M. Sugi, and Y. Ozaki, "New correlation indices invariant to band shifts in generalized two-dimensional correlation infrared spectroscopy," *Chemical physics letters*, vol. 402, no. 1-3, pp. 251–257, 2005.

[5] O. Zavorotynska, S. Deledda, G. Li, M. Matsuo, S.-i. Orimo, and B. C. Hauback, "Isotopic exchange in porous and dense magnesium borohydride," *Angewandte Chemie International Edition*, vol. 54, no. 36, pp. 10 592–10 595, 2015.

[6] S. R. Batten, N. R. Champness, X.-M. Chen, J. Garcia-Martinez, S. Kitagawa, L. Öhrström, M. O'Keeffe, M. P. Suh, and J. Reedijk, "Terminology of metal–organic frameworks and coordination polymers (iupac recommendations 2013)," *Pure and Applied Chemistry*, vol. 85, no. 8, pp. 1715–1724, 2013.

[7] H.-Q. Zheng, C.-Y. Liu, X.-Y. Zeng, J. Chen, J. Lu+, R.-G. Lin, R. Cao, Z.-J. Lin, and J.-W. Su, "Mof-808: a metal–organic framework with intrinsic peroxidase-like catalytic activity at neutral ph for colorimetric biosensing," *Inorganic chemistry*, vol. 57, no. 15, pp. 9096–9104, 2018.

[8] I. Noda, A. Dowrey, C. Marcott, G. Story, and Y. Ozaki, "Generalized two-dimensional correlation spectroscopy," *Applied Spectroscopy*, vol. 54, no. 7, pp. 236A–248A, 2000.

[9] L. Zuo, S.-q. Sun, Q. Zhou, J.-x. Tao, and I. Noda, "2d-ir correlation analysis of deteriorative process of traditional chinese medicine 'qing kai ling'injection," *Journal of Pharmaceutical and Biomedical analysis*, vol. 30, no. 5, pp. 1491–1498, 2003.

[10] "Raman imaging & spectroscopy analysis." [Online]. Available: https://www.horiba.com/int/scientific/technologies/raman-imaging-and-spectroscopy/raman-analysis/

[11] K. Nakamoto, *Infrared and Raman spectra of inorganic and coordination compounds, part B: applications in coordination, organometallic, and bioinorganic chemistry*. John Wiley & Sons, 2009.

[12] M. Raza, J. Houston, R. Geleit, R. Williams, and A. Trompeter, "The use of ionising radiation in orthopaedic surgery: principles, regulations and managing risk to surgeons and patients," *European Journal of Orthopaedic Surgery & Traumatology*, vol. 31, no. 5, pp. 947–955, 2021.

[13] J. M. Hollas, *Modern spectroscopy*. John Wiley & Sons, 2004.

[14] "Amplitude," Jul 2017. [Online]. Available: http://www.msrblog.com/science/physics/amplitude.html

[15] R. L. McCreery, *Raman spectroscopy for chemical analysis*. John Wiley & Sons, 2005, vol. 225.

[16] "What must happen for an electron to move to a higher energy level?: Socratic," Nov 2015. [Online]. Available: https://socratic.org/questions/what-must-happen-for-an-electron-to-move-to-a-higher-energy-level

[17] M. Hesse, H. Meier, and B. Zeeh, *Spektroskopische Methoden in der organischen Chemie*. Georg Thieme Verlag, 2005.

[18] "Raman spectroscopy," May 2022. [Online]. Available: https://en.wikipedia.org/wiki/Raman_spectroscopy

[19] Y. C. Cho and S. I. Ahn, "Fabricating a raman spectrometer using an optical pickup unit and pulsed power," *Scientific reports*, vol. 10, no. 1, pp. 1–8, 2020.

[20] J. Wiley *et al.*, *Sons*. Inc New York; NY, 2001, vol. 1, no. 11.

[21] E. Vargis, Y.-W. Tang, D. Khabele, and A. Mahadevan-Jansen, "Near-infrared raman microspectroscopy detects high-risk human papillomaviruses," *Translational Oncology*, vol. 5, no. 3, pp. 172–179, 2012.

[22] N. Egeland, "Raman spectroscopy applied to enhanced oil recovery research," Master's thesis, University of Stavanger, Norway, 2015.

[23] R. Černỳ, Y. Filinchuk, H. Hagemann, and K. Yvon, "Magnesium borohydride: synthesis and crystal structure," *Angewandte Chemie*, vol. 119, no. 30, pp. 5867–5869, 2007.

[24] O. Zavorotynska, A. El-Kharbachi, S. Deledda, and B. C. Hauback, "Recent progress in magnesium borohydride mg (bh4) 2: Fundamentals and applications for energy storage," *international journal of hydrogen energy*, vol. 41, no. 32, pp. 14 387–14 403, 2016.

[25] R. A. Novelline and L. F. Squire, *Squire's fundamentals of radiology*. La Editorial, UPR, 2004.

[26] Y. Waseda, E. Matsubara, and K. Shinoda, *X-ray diffraction crystallography: introduction, examples and solved problems*. Springer Science & Business Media, 2011.

[27] C. Kittel, "Introduction to solid state physics, new york, john wiley& sons," *Inc., 195b*, 2005.

[28] W. H. Bragg, "Ix. bakerian lecture.—x-rays and crystal structure," *Philosophical Transactions of the Royal Society of London. Series A, Containing Papers of a Mathematical or Physical Character*, vol. 215, no. 523-537, pp. 253–274, 1915.

[29] R. Reynolds, "The lorentz-polarization factor and preferred orientation in oriented clay aggregates," *Clays and Clay Minerals*, vol. 34, no. 4, pp. 359–367, 1986.

[30] J. Redfern and A. Coats, "Thermogravimetric analysis," *Analys*, vol. 88, pp. 906–924, 1963.

[31] X. Liu and W. Yu, "Evaluating the thermal stability of high performance fibers by tga," *Journal of applied polymer science*, vol. 99, no. 3, pp. 937–944, 2006.

[32] J. Jehlička, H. Edwards, and A. Culka, "Using portable raman spectrometers for the identification of organic compounds at low temperatures and high altitudes: exobiological applications," *Philosophical Transactions of the Royal Society A: Mathematical, Physical and Engineering Sciences*, vol. 368, no. 1922, pp. 3109–3125, 2010.

[33] A. Nejad, K. A. Meyer, F. Kollipost, Z. Xue, and M. A. Suhm, "Slow monomer vibrations in formic acid dimer: Stepping up the ladder with ftir and raman jet spectroscopy," *The Journal of Chemical Physics*, vol. 155, no. 22, p. 224301, 2021.

[34] K. I. Hadjiivanov, D. A. Panayotov, M. Y. Mihaylov, E. Z. Ivanova, K. K. Chakarova, S. M. Andonova, and N. L. Drenchev, "Power of infrared and raman spectroscopies to characterize metal-organic frameworks and investigate their interaction with guest molecules," *Chemical Reviews*, vol. 121, no. 3, pp. 1286–1424, 2020.

[35] J. Li, Z. Zhao, P. Ren, C. Sun, and M. Zhou, "Covalent symmetrization of the hexagonal networks of trimesic acids at high pressure," *Optik*, vol. 127, no. 13, pp. 5396–5399, 2016.

[36] K. L. Miller, J. L. Falconer, and J. W. Medlin, "Effect of water on the adsorbed structure of formic acid on tio2 anatase (1 0 1)," *Journal of catalysis*, vol. 278, no. 2, pp. 321–328, 2011.

[37] K. Kumar and S. Murugesan, "Synthesis, characterization and anti-bacterial activity of divalent transition metal complexes of hydrazine and trimesic acid," *Journal of Saudi Chemical Society*, vol. 22, no. 1, pp. 16–26, 2018.

[38] K. Xuan, Y. Pu, F. Li, J. Luo, N. Zhao, and F. Xiao, "Metal-organic frameworks mof-808-x as highly efficient catalysts for direct synthesis of dimethyl carbonate from co2 and methanol," *Chinese Journal of Catalysis*, vol. 40, no. 4, pp. 553–566, 2019.

[39] J. Feng, Y. Zhong, M. Xie, M. Li, and S. Jiang, "Using mof-808 as a promising support to immobilize ru for selective hydrogenation of levulinic acid to γ-valerolactone," *Catalysis Letters*, vol. 151, no. 1, pp. 86–94, 2021.

[40] T. J. Demars, M. K. Bera, S. Seifert, M. R. Antonio, and R. J. Ellis, "Revisiting the solution structure of ceric ammonium nitrate," *Angewandte Chemie International Edition*, vol. 54, no. 26, pp. 7534–7538, 2015.

[41] X. Chen, E. Yu, S. Cai, H. Jia, J. Chen, and P. Liang, "In situ pyrolysis of ce-mof to prepare ceo2 catalyst with obviously improved catalytic performance for toluene combustion," *Chemical Engineering Journal*, vol. 344, pp. 469–479, 2018.

[42] G. Mahalakshmi and V. Balachandran, "Ft-ir and ft-raman spectra, normal coordinate analysis and ab initio computations of trimesic acid," *Spectrochimica Acta Part A: Molecular and Biomolecular Spectroscopy*, vol. 124, pp. 535–547, 2014.

[43] I. Nakagawa and J. Walter, "Optically active crystal vibrations of the alkali-metal nitrates," *The Journal of Chemical Physics*, vol. 51, no. 4, pp. 1389–1397, 1969.

[44] I. Das, M. T. Noori, M. Shaikh, M. M. Ghangrekar, and R. Ananthakrishnan, "Synthesis and application of zirconium metal–organic framework in microbial fuel cells as a cost-effective oxygen reduction catalyst with competitive performance," *ACS Applied Energy Materials*, vol. 3, no. 4, pp. 3512–3520, 2020.

[45] F. Herbstein, M. Kapon, I. Maor, and G. Reisner, "The structure of trimesic acid, its hydrates and complexes. vi. glycine–trimesic acid monohydrate, h3n+ ch2coo-. c9h6o6. h2o," *Acta Crystallographica Section B: Structural Crystallography and Crystal Chemistry*, vol. 37, no. 1, pp. 136–140, 1981.

[46] T. A. Beineke and J. Delgaudio, "Crystal structure of ceric ammonium nitrate," *Inorganic chemistry*, vol. 7, no. 4, pp. 715–721, 1968.

[47] R. Muruganantham, Y.-J. Gu, Y.-D. Song, C.-W. Kung, and W.-R. Liu, "Ce-mof derived ceria: Insights into the na-ion storage mechanism as a high-rate performance anode material," *Applied Materials Today*, vol. 22, p. 100935, 2021.

[48] G. Jayakumar, A. A. Irudayaraj, and A. D. Raj, "Particle size effect on the properties of cerium oxide (ceo2) nanoparticles synthesized by hydrothermal method," *Mechanics, Materials Science & Engineering Journal*, vol. 9, no. 1, 2017.

[49] M. N. Pervez, C. Chen, Z. Li, V. Naddeo, and Y. Zhao, "Tuning the structure of cerium-based metal-organic frameworks for efficient removal of arsenic species: The role of organic ligands," *Chemosphere*, p. 134934, 2022.

[50] Y. Park, S. M. Kim, S. Jin, S. M. Lee, I. Noda, and Y. M. Jung, "Investigation of the phase transition mechanism in lifepo4 cathode using in situ raman spectroscopy and 2d correlation spectroscopy during initial cycle," *Molecules*, vol. 24, no. 2, p. 291, 2019.

Appendix A

R script

A.1 Coding for red laser

```
library(corr2D)
Matrix3 <- read.csv("Matrix2.csv")
Matrix1<-Matrix2[which(Matrix2[,1]>200 & Matrix4[,1]<2000),] #choose the range
myMatrix<-t(Matrix1)
X<-myMatrix[1,]
colnames(myMatrix) <- X
myMatrix4< −myMatrix[c(1,2,3,4,5,6),] #change the waves
twod < −corr2d(myMatrix4,scaling = 1) #choose scaling between 0, 0.5, 1
plot-corr2d(twod)
plot(twod,Im(twod$FT))
```

A.2 Coding for green laser

```
library(corr2D)
Matrix3 <- read.csv("Matrix4.csv")
Matrix1<-Matrix4[which(Matrix4[,1]>400 & Matrix4[,1]<1800),] #choose the range
myMatrix<-t(Matrix1)
X<-myMatrix[1,]
colnames(myMatrix) <- X
myMatrix4< −myMatrix[c(1,2,3,4,5,6,7,8,9),] #change the waves
twod < −corr2d(myMatrix4,scaling = 1) #choose scaling between 0, 0.5, 1
plot-corr2d(twod)
plot(twod,Im(twod$FT))
```

A.3 Coding for $Mg(BH_4)_2$

```
library(corr2D)
Matrix6 <- read.csv("Matrix6.csv")
Matrix6 <- Matrix6[which(Matrix6[, 1] > 1500 & Matrix6[, 1] < 2500), ] #choose the range
myMatrix <- t(Matrix6)
X <- myMatrix[1, ]
myMatrix <- myMatrix[-1, ]
colnames(myMatrix) <- X
myMatrix4 <- myMatrix
dim(myMatrix4)
twod <- corr2d(myMatrix4, scaling = 0) #choose scaling between 0, 0.5, 1
plot_corr2d(twod)
#plot(twod,Im(twod$FT))
```